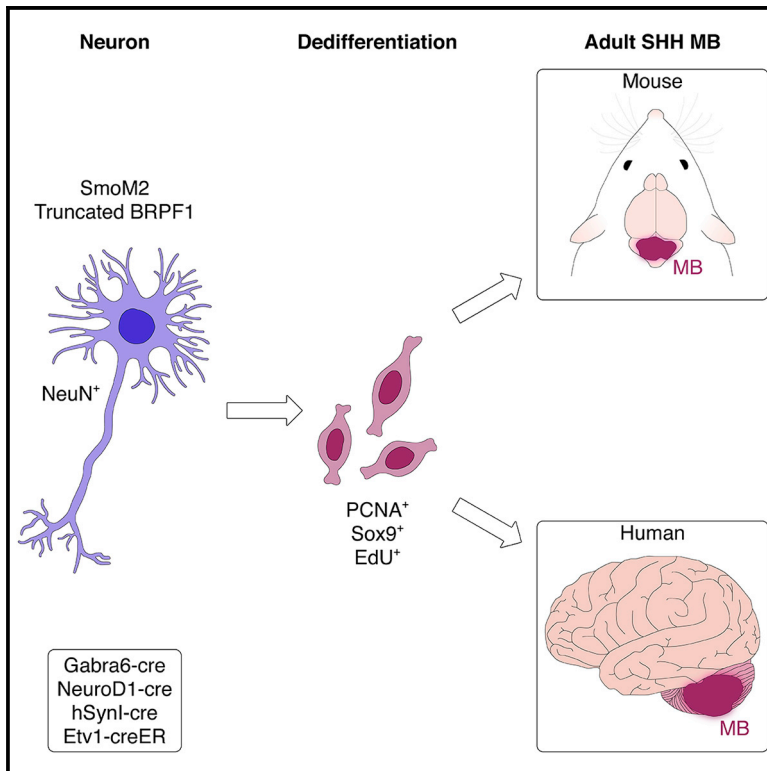


Truncated BRPF1 Cooperates with Smoothened to Promote Adult Shh Medulloblastoma

Graphical Abstract



Authors

Giuseppe Aiello, Claudio Ballabio, Riccardo Ruggeri, ..., Alessandro Romanel, Alessio Zippo, Luca Tiberi

Correspondence

luca.tiberi@unitn.it

In Brief

Medulloblastoma is a brain tumor affecting the cerebellum of infants and adults. Aiello et al. establish a mouse model for adult onset, which allows investigation of the pathogenesis of the disease and identifies neurons as putative cells of origin.

Highlights

- SmoM2 overexpression promotes cerebellar granule neurons dedifferentiation *in vivo*
- SmoM2 and mutant BRPF1 cooperation *in vivo* mimics human adult SHH MBs
- Granule neurons are putative cells of origin of adult SHH MBs
- Truncated BRPF1 increases the accessibility of a subset of super-enhancers



Truncated BRPF1 Cooperates with Smoothened to Promote Adult Shh Medulloblastoma

Giuseppe Aiello,¹ Claudio Ballabio,¹ Riccardo Ruggeri,¹ Luca Fagnocchi,² Marica Anderle,¹ Ilaria Morassut,¹ Davide Caron,¹ Francesca Garilli,¹ Francesca Gianni,^{3,4} Felice Giangaspero,^{3,4} Silvano Piazza,⁵ Alessandro Romanel,⁶ Alessio Zippo,² and Luca Tiberi^{1,7,*}

¹Armenise-Harvard Laboratory of Brain Disorders and Cancer, CIBIO, University of Trento, Via Sommarive 9, 38123 Trento, Italy

²Laboratory of Chromatin Biology & Epigenetics, CIBIO, University of Trento, Via Sommarive 9, 38123 Trento, Italy

³Department of Radiologic, Oncologic and Anatomic Pathological Sciences, University Sapienza of Rome, Rome, Italy

⁴IRCCS Neuromed, Pozzilli, Isernia, Italy

⁵Bioinformatics Core Facility, CIBIO, University of Trento, Via Sommarive 9, 38123 Trento, Italy

⁶Laboratory of Bioinformatics and Computational Genomics, CIBIO, University of Trento, Via Sommarive 9, 38123 Trento, Italy

⁷Lead Contact

*Correspondence: luca.tiberi@unitn.it

<https://doi.org/10.1016/j.celrep.2019.11.046>

SUMMARY

The transition of neural progenitors to differentiated postmitotic neurons is mainly considered irreversible in physiological conditions. In the present work, we show that Shh pathway activation through SmoM2 expression promotes postmitotic neurons dedifferentiation, re-entering in the cell cycle and originating medulloblastoma *in vivo*. Notably, human adult patients present inactivating mutations of the chromatin reader BRPF1 that are associated with SMO mutations and absent in pediatric and adolescent patients. Here, we found that truncated BRPF1 protein, as found in human adult patients, is able to induce medulloblastoma in adult mice upon SmoM2 activation. Indeed, postmitotic neurons re-entered the cell cycle and proliferated as a result of chromatin remodeling of neurons by BRPF1. Our model of brain cancer explains the onset of a subset of human medulloblastoma in adult individuals where granule neuron progenitors are no longer present.

INTRODUCTION

Tumors are composed of proliferating cells that invade healthy tissue and grow over time. Even though it is still unclear, it is a common opinion that the cells of origin should possess a proliferative capacity (Blanpain, 2013; Visvader, 2011). The transition of neural progenitors to differentiated postmitotic neurons is considered irreversible in physiological and pathological conditions (Deneris and Hobert, 2014; Nguyen et al., 2006). Therefore, postmitotic neurons have not been considered as suitable cells of origin of brain cancer. Interestingly, few groups have attempted to induce cancer from neurons using full knockout (KO) mice for cell-cycle regulators or by genetic modification of mice and *Drosophila melanogaster* (Ajioka et al., 2007; Friedmann-Morvinski et al., 2012; Southall et al., 2014). Furthermore, it is still unclear whether this process could be relevant to human brain

cancer formation. For instance, human SHH medulloblastoma (MB) is a brain tumor found in adults and infants that is thought to originate from cerebellar granule neuron progenitors. Notably, several groups have shown that Shh pathway activation (SmoM2 overexpression) in mouse granule neuron progenitors is able to induce Shh MB (Schüller et al., 2008; Yang et al., 2008). These progenitors are present in infants and newborn mice, but they seem not to be present in adult humans and mice (Marzban et al., 2015; Yang et al., 2008), therefore suggesting that adult MB could originate from a different subset of cells. Based on these data, we speculate that postmitotic neurons are the cells of origin of adult SHH MBs. Interestingly, several adult SHH MB patients present truncated mutations of the chromatin reader BRPF1 that are often associated with Smoothened (SMO) mutations and completely absent in pediatric and adolescent patients (Kool et al., 2014). Therefore, we investigate whether BRPF1 mutations could be required to allow tumor formation in adult patients.

RESULTS

SmoM2 Expression in Granule Neurons Promotes MB

In the present work, we investigated if postmitotic neurons could dedifferentiate *in vivo* and if this process could lead to Shh MB in mice. To do so, we induced Shh pathway activation through the expression of a constitutively active Smo mutant (SmoM2) to mimic the SMO gain of function mutations present in human adult SHH MB (Kool et al., 2014; Northcott et al., 2012). In particular, to examine if neurons can dedifferentiate *in vivo*, we conditionally induced SmoM2-EYFP expression (*LSL-SmoM2* mice) in postmitotic neurons using *Gabra6-cre* mouse (Aller et al., 2003). Indeed, GABAA receptor $\alpha 6$ subunit (*Gabra6*) is expressed only in postmitotic neurons and it has already been shown that *Gabra6-cre* mouse induces recombination in neurons of the cerebellum, midbrain, and cortex. As shown in Figures 1A and 1B, *Gabra6-cre;LSL-SmoM2* mice developed MBs (7 and 4 months) and showed signs of ataxia, frequent falls, and weight loss ($n = 9$). Moreover, Kaplan-Meier survival analysis showed that less than 50% of the mice were still alive after 300 days (Figure 1C). Notably, we found



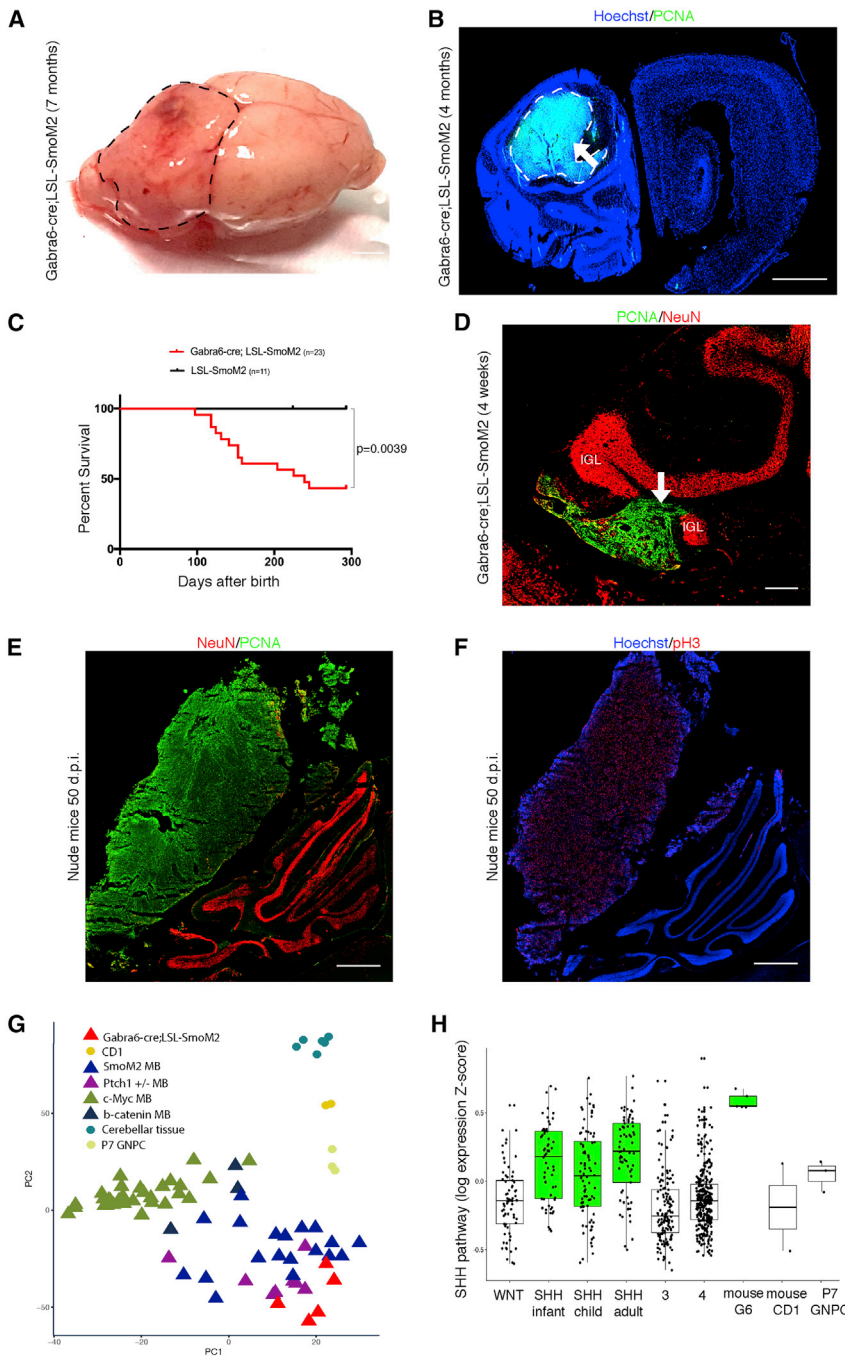


Figure 1. SmoM2 Expression in Granule Neurons Promotes Shh MB

(A) Image of 7-month-old *Gabra6-cre;LSL-SmoM2* MB.

(B) Hoechst and PCNA staining of brain section of 4-month-old *Gabra6-cre;LSL-SmoM2* mouse. The arrow points to the tumor.

(C) Kaplan-Meier survival curves of *LSL-SmoM2* and *Gabra6-cre;LSL-SmoM2* mice.

(D and E) PCNA and NeuN staining of brain sections of 4-week-old *Gabra6-cre;LSL-SmoM2* mouse (D) and 4-month-old nude mice, 50 days post injection (d.p.i.), with *Gabra6-cre;LSL-SmoM2* MB cells (E); arrow points to the tumor. Lower and higher magnifications of (D) are shown in Figures S1AK and S1AL.

(F) Hoechst and pH3 staining of brain sections of 4-month-old nude mice, 50 d.p.i., with *Gabra6-cre;LSL-SmoM2* MB cells.

(G) Multidimensional scaling of several MB mouse models, plotting the results of the two principal coordinates. Original GEO dataset entries (GEO: GSE11859, GSE24628, and GSE33199). PC1, principal coordinate 1; PC2, principal coordinate 2.

(H) Boxplots of the median values of the Shh genes for the human samples (GEO: GSE85217) and *Gabra6-cre;LSL-SmoM2* MB. CD1, normal cerebellum tissue; G6, *Gabra6-cre;LSL-SmoM2*; SHH, SHH subgroup; WNT, WNT subgroup; 3, group 3; 4, group 4; P7 GNPC, P7 granule neuron progenitors cell.

Scale bars, 2 mm in (A), 1 mm in (B), (E), and (F), and 250 μ m (D). The dashed lines in (A) and (B) mark the tumors. d.p.i., days post injection.

cerebellum aberrations and presence of tumor cells expressing PCNA, a marker of cell proliferation, as early as in 4-week-old mice (Figure 1D). The tumor localization suggests that it could originate from neurons of the EGL (external granular layer), IGL (internal granular layer), or the molecular layer. Several cells within the tumor were also Sox9 (Figures S1A, S1B, and S1E) and Sox2 positive (Figures S1C, S1D, and S1E), two cell markers present in mouse and human SHH MBs (Sutter et al., 2010; Swartling et al., 2012; Vanner et al., 2014) and expressed

at higher levels in human adult SHH MBs, compared to the infant form (Al-Halabi et al., 2011). Notably, Sox2 and Sox9 proteins are also expressed in mouse neural stem cells, Bergmann glia cells, and at low levels in granule neuron progenitors during cerebellum development (Ahlfeld et al., 2013; Sutter et al., 2010; Vong et al., 2015). The tumors were also positive for doublecortin (Dcx), a marker for highly proliferative progenitors present in mouse Shh MBs (Figure S1F). The tumors were EYFP positive (GFP antibody), thus confirming that SmoM2-EYFP is expressed in cancer cells (Figure S1G). Furthermore, histopathological and immunophenotypic analyses confirmed that tumors in *Gabra6-cre;LSL-SmoM2* mice are Shh MBs (Yap1 and Gab1 positive and with cytoplasmic beta-catenin) (Ellison et al., 2011) (Figures S1I–S1R). In our search for putative genes required for neuron dedifferentiation, we crossed *Gabra6-cre;LSL-SmoM2* mice with *Sox9^{flox}* mice. In fact, it has already been shown that SmoM2 requires Sox9 to induce basal cell carcinoma (skin cancer) (Larsimont et al., 2015). Interestingly, we also obtained MBs in *Gabra6-cre;LSL-SmoM2;Sox9^{flox/flox}* mice (3/3 mice; Figure S1H),

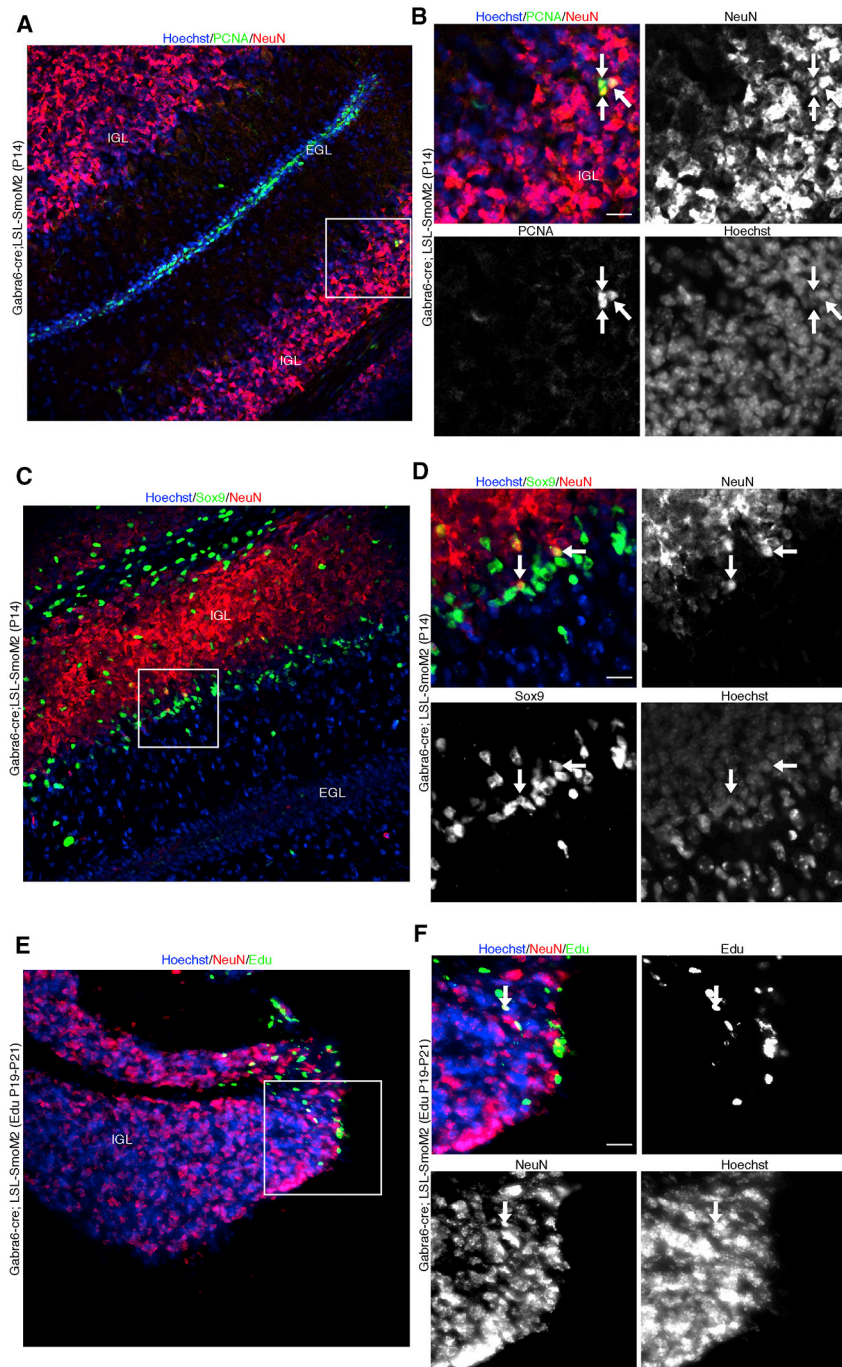


Figure 2. SmoM2 Promotes Dedifferentiation of Granule Neurons

(A and B) Hoechst, PCNA, and NeuN staining of brain sections of P14 *Gabra6-cre;LSL-SmoM2* mouse. Square in (A) marks the region shown at higher magnification in (B). Arrows point to PCNA/NeuN double-positive cells.

(C and D) Hoechst, Sox9, and NeuN staining of brain sections of P14 *Gabra6-cre;LSL-SmoM2* mouse. Square in (C) marks the region shown at higher magnification in (D). Arrows point to Sox9/NeuN double-positive cells.

(E and F) Hoechst, Edu, and NeuN staining of brain sections of P21 *Gabra6-cre;LSL-SmoM2* mouse, injected with Edu at P19. Square in (E) marks the region shown at higher magnification in (F). Lower magnification of (E) is shown in [Figure S2Q](#). Arrows point to Edu/NeuN double-positive cells.

Scale bars, 25 μ m in (B), (D), and (F). EGL, external granular layer; IGL, internal granular layer.

([Figures 1E and 1F](#); data not shown). To further characterize our mouse model, we examined the expression profiles of five different *Gabra6-cre;LSL-SmoM2* MBs and compared them to wild-type (WT) cerebellar tissue obtained from CD1 mice. In particular after determining the differentially expressed genes ([Table S1](#)), we performed functional annotation procedures using the Database for Annotation, Visualization and Integrated Discovery (DAVID) and gene set enrichment analysis (GSEA). As shown in [Figures S1S and S1T](#), the tumor samples presented an increase in the expression of genes linked to cell cycle, DNA replication, and as expected to the Shh pathway. Consistently, we observed a decreased expression of genes related to normal neuron functions like the synaptic vesicles cycle ([Figure S1T](#)). We then compared our model to several types of MB mouse models using publicly available datasets (GEO: GSE11859, GSE24628, and GSE33199). PCA analysis showed that the gene expression profile of tumors retrieved from *Gabra6-cre;LSL-SmoM2* clustered with *SmoM2*

indicating that Sox9 functions are not conserved between skin and brain cancer. To further confirm the tumorigenicity of *Gabra6-cre;LSL-SmoM2* MB cells, we performed tumor transplantation experiments. Specifically, we isolated cells from 4-month-old tumor-bearing *Gabra6-cre;LSL-SmoM2* cerebella and then we injected the cells into the cerebellum of 4-month-old nude mice (*Foxn1^{nu}*). Our results showed that all four mice injected with *Gabra6-cre;LSL-SmoM2* MB cells generated tumors populated by PCNA, NeuN, and pH 3 positive cells

and *Ptch1^{+/-}* Shh MB mouse models ([Figure 1G](#)). Finally, we compared our model to human SHH MB gene expression dataset (GEO: GSE85217), with respect to the enrichment of the SHH pathway signature. This analysis showed that *Gabra6-cre;LSL-SmoM2* (G6) samples activated the SHH pathway to the same extent as human SHH MBs ([Figure 1H](#)). Together, these results are consistent with the hypothesis that *Gabra6-cre;LSL-SmoM2* represents a putative Shh MB mouse model.

SmoM2 Promotes Dedifferentiation of Granule Neurons

Our data suggest that Smo gain of function in postmitotic neurons is sufficient to induce MB formation and reinforce the possibility that neurons are dedifferentiating. To clarify if the granule neurons started dedifferentiating at early stages of tumor formation, we analyzed *Gabra6-cre;LSL-SmoM2* mice at postnatal day 14 (P14). As shown in Figures 2A and 2B, few PCNA and NeuN double-positive cells can be detected at this stage in mouse cerebellum (33 ± 8 cells in three sections for each brain, mean \pm SD, $n = 4$ brains), indicating that neurons have started to proliferate without losing NeuN expression. Notably, we did not observe PCNA and NeuN double-positive cells in control mice (*LSL-SmoM2*) (Figure S1H; data not shown), therefore indicating that SmoM2 induction upon cre expression was responsible for this proliferation burst. This suggests that the PCNA and NeuN double-positive cells could represent the cell of origin of Shh MBs. Interestingly, we also identified Sox9/Sox2 and NeuN double-positive cells, indicating that some neurons while dedifferentiating start expressing markers of neuronal progenitors (Figures 2C, 2D, S1U, and S1V). Of notice, the same phenotype was not observed in control mice (Figure S1H). Indeed, it has been published that rare Sox2-expressing cells are the founding cancer stem cell population driving cancer initiation and therapy resistance (Vanner et al., 2014) in mouse models of infant Shh MBs. Based on this knowledge, we analyzed the *Gabra6-cre;LSL-SmoM2* mice at different time points and we detected Sox9/PCNA and NeuN double-positive cells at P7, P14, P21, and P28 (Figures S1W–S1AD and S1AE–S1AL). Notably, at P21 we already observed small clusters of PCNA-positive cells (Figures S1AI and S1AJ) and aberrant Sox9 expression (Figures S1AA and S1AB). SmoM2 expression was confirmed by immunofluorescence using a GFP antibody that recognizes the YFP fused to SmoM2 (Figures S1AM–S1AP). To better detect and identify dedifferentiated neurons, we crossed the *Gabra6-cre;LSL-SmoM2* mice with *LSL-tdTomato* mice that express tdTomato only upon cre recombination (Madisen et al., 2010). As shown in Figures S2A–S2L, we did not observe tdTomato expression in mice embryos at embryonic day 16.5 (E16.5) (*Gabra6-cre;LSL-SmoM2;LSL-tdTomato*), but we detected PCNA/Sox9 and tdTomato double-positive cells in the IGL at P7 and P14, when granule neurons are already present. Since *Gabra6-cre* mice express cre recombinase also in few deep cerebellar nuclei (DCN) cells (Aller et al., 2003), we analyzed PCNA expression in *Gabra6-cre;LSL-tdTomato* and *Gabra6-cre;LSL-SmoM2* in DCN. Notably, we did not detect any aberrant PCNA staining at P21 in both mice (Figures S2M–S2P). Therefore, we postulate that the tumors should not originate from dedifferentiated neurons of DCN. Taken together, these data suggest that the Sox2/Sox9 and NeuN double-positive cells identified in the cerebellum of *Gabra6-cre;LSL-SmoM2* mice could be dedifferentiated granule neurons that originate Shh MB. To further confirm our hypothesis, we injected EdU in *Gabra6-cre;LSL-SmoM2* mice at P19 to avoid EdU incorporation in progenitors (that are not present at this time point) and to label only neurons that re-enter in the cell cycle. As shown in Figures 2E, 2F, and S2Q, we observed small clusters of EdU-positive cells in the IGL at P21 *Gabra6-cre;LSL-SmoM2* mice and not in *Gabra6-cre;LSL-tdTomato* mice (Figures S2R and S2S–S2AC). Therefore, we

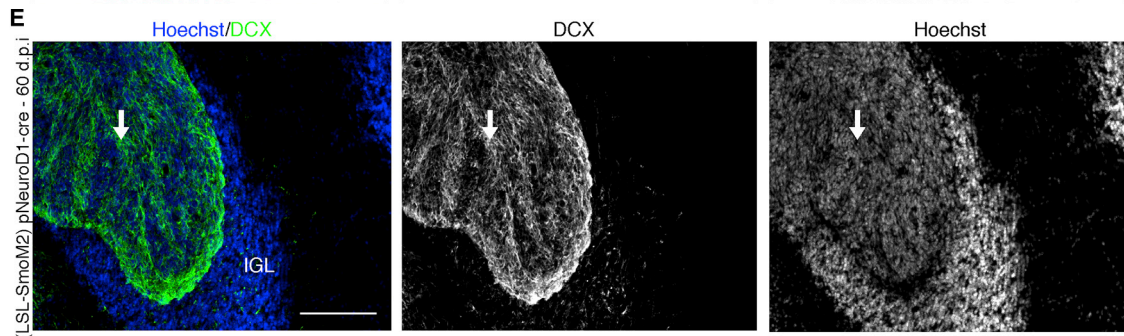
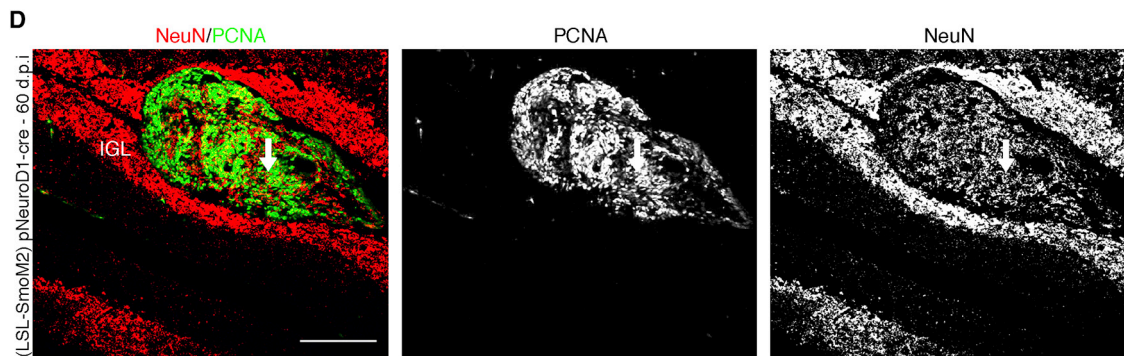
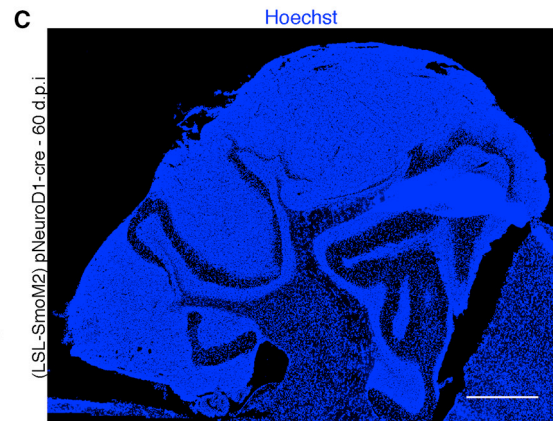
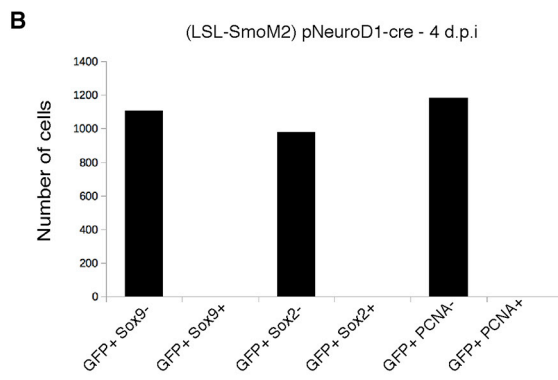
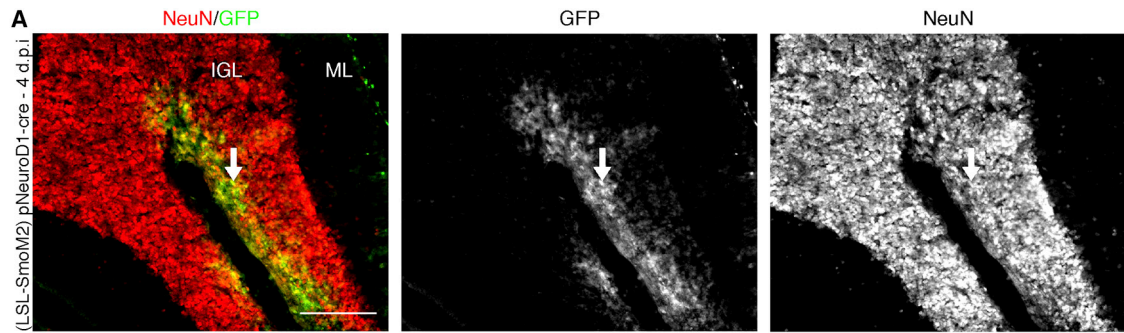
speculate that the EdU-positive cells could be dedifferentiated neurons. Since Ptch1 ablation in cerebellar progenitors is able to induce Shh MB in a few months (Northcott et al., 2012), we analyzed the effect of Ptch1 loss in postmitotic neurons in *Gabra6-cre;Ptch1^{fllox/fllox}* and *Gabra6-cre;Ptch1^{fllox/+}* mice, but we did not observe MB development (Figure S1H). To understand the reason why SmoM2 overexpression, unlike Ptch1 deletion, leads to tumor formation, we analyzed their cerebella at P14 by quantitative real-time PCR. As shown previously, at this stage most of the granule neurons have been produced and in *Gabra6-cre;LSL-SmoM2* there is no tumor formation yet. Gene expression analysis revealed that *Math1* and *Gli1* genes are upregulated specifically in *Gabra6-cre;LSL-SmoM2* mice, but not in *Gabra6-cre;Ptch1^{fllox/fllox}* (Figure S3A). These data suggest that SmoM2 overexpression induces a much stronger activation of Shh signaling and *Math1* (specific marker for granule neuron progenitors) as compared to Ptch1 loss and could explain the presence of Shh MBs in *Gabra6-cre;LSL-SmoM2* and its absence in *Gabra6-cre;Ptch1^{fllox/fllox}* mice. It has also been shown that *Ptch1^{fllox}* mice are able to induce MB when crossed with mice expressing recombinase in cerebellar progenitors (*GFAP-cre*) (Wu et al., 2017) and we validated the effect of Ptch1 deletion in *Math1-creER;Ptch1^{fllox/+}* mice, observing the induction of progenitors overproliferation (Figures S3B and S3C).

Gabra6-Cre Mice Express Cre Recombinase in Neurons

To exclude that *Gabra6-cre* mice induce recombination in cerebellar progenitors, we crossed them with *LSL-tdTomato* mice that express tdTomato only upon cre recombination. We then analyzed if tdTomato was expressed in progenitors at different postnatal time points. We quantified several thousand tdTomato positive cells (see STAR Methods) and all of them were negative for progenitors, glial or proliferation markers such as PCNA, pH3, Sox2, and Sox9 (Figures S3D–S3L). Moreover, almost all tdTomato cells were positive for the neuronal marker NeuN at P4, P7, P10, and P14 (Figure S3L). Finally, to confirm the specificity of *Gabra6-cre;LSL-tdTomato* mice, we crossed them with *Math1-GFP* mice that express a *Math1* protein fused with GFP (Rose et al., 2009) only in granule neuron progenitors. As shown in Figures S4A–S4E, tdTomato-positive cells were GFP negative. Interestingly, in *Gabra6-cre;LSL-tdTomato* mice, tdTomato was expressed in several brain regions such as the cortex, hippocampus, ventral thalamus, and hypothalamus (Figures S4F–S4J). Taken together, these data indicate that our genetic model allows manipulation of postmitotic neurons only. Moreover, these data suggest that only cerebellar neurons are able to dedifferentiate into cancer cells, since we have never observed tumor masses in other regions of the brain.

Transient Cre Recombinase Expression Promotes Dedifferentiation of Granule Neurons in LSL-SmoM2 Mice

To prove that Shh MB originates from postmitotic neurons, we transfected granule neurons of *LSL-SmoM2* mice at P21/P24 with a plasmid expressing cre recombinase under the control of NeuroD1 promoter (pNeuroD1-cre) (Guerrier et al., 2009). NeuroD1 is expressed in granule neurons and progenitors (Cho and Tsai, 2006), but at the selected time points granule neuron



F

Genotype	pNeuroD1cre transfection	
	Aberrant PCNA	Tumors
WT	0/2	0/2
SmoM2	5/16	1/16

(legend on next page)

progenitors are no longer present (Tiberi et al., 2014; Yang et al., 2008) (Figure S4K). As shown in Figure 3A, 4 days after *in vivo* transfection of pNeuroD1-cre-IRES-GFP, we detected GFP-positive cells in the cerebellum IGL, but we did not detect Sox9/Sox2/PCNA and GFP double-positive cells (Figures 3B and S4L–S4O). These data suggest that we can specifically transfect cerebellar neurons. Anyhow, it has been shown by other groups that Shh pathway activation in granule neuron progenitors after P12–P14 does not lead to MB formation (Yang et al., 2008). We have confirmed these data by induction of SmoM2 with a granule neuron progenitor specific promoter (*Math1-creER*) at P21 and we did not obtain MB (Figure S1H). On the contrary, as shown in Figure 3C, 60 days after pNeuroD1-cre transfection at P21, we observed MB in only one mouse (n = 16). Furthermore, we noticed the formation of PCNA, DCX, pH3, Sox2, and Sox9 positive cells clusters in the IGL of five other mice (Figures 3D–3F and S4P–S4R). These data suggest that SmoM2 expression driven by pNeuroD1-cre in mouse cerebellum (when granule neuron progenitors are not present) can rarely induce Shh MB. In addition, we investigated the possibility to dedifferentiate neurons in adult mice. We transfected 2-month-old *LSL-SmoM2* mice with a plasmid expressing cre recombinase under the control of human Synapsin1 promoter (*phSyn1-cre*). This promoter has been shown to induce expression of desired genes in postmitotic neurons and not in glial cells (Kügler et al., 2003). Indeed, 4 days after *in vivo* transfection of *phSyn1-cre* together with pPB-LSL-tdTomato in 2-month-old *LSL-SmoM2* mice, we did not detect Sox9/Sox2/PCNA/pH3 and tdTomato double-positive cells (Figures S4S–S4U). As shown in Figures S5A and S5B, we obtained formation of abnormal PCNA and Sox9 clusters in cerebellum IGL (upon SmoM2 expression) in two out of seven transfected adult mice. These clusters are positive for GFP staining, indicating that transfected cells are expressing SmoM2-YFP. Taken together, these data suggest that SmoM2 is also able to dedifferentiate granule neurons in adult mice.

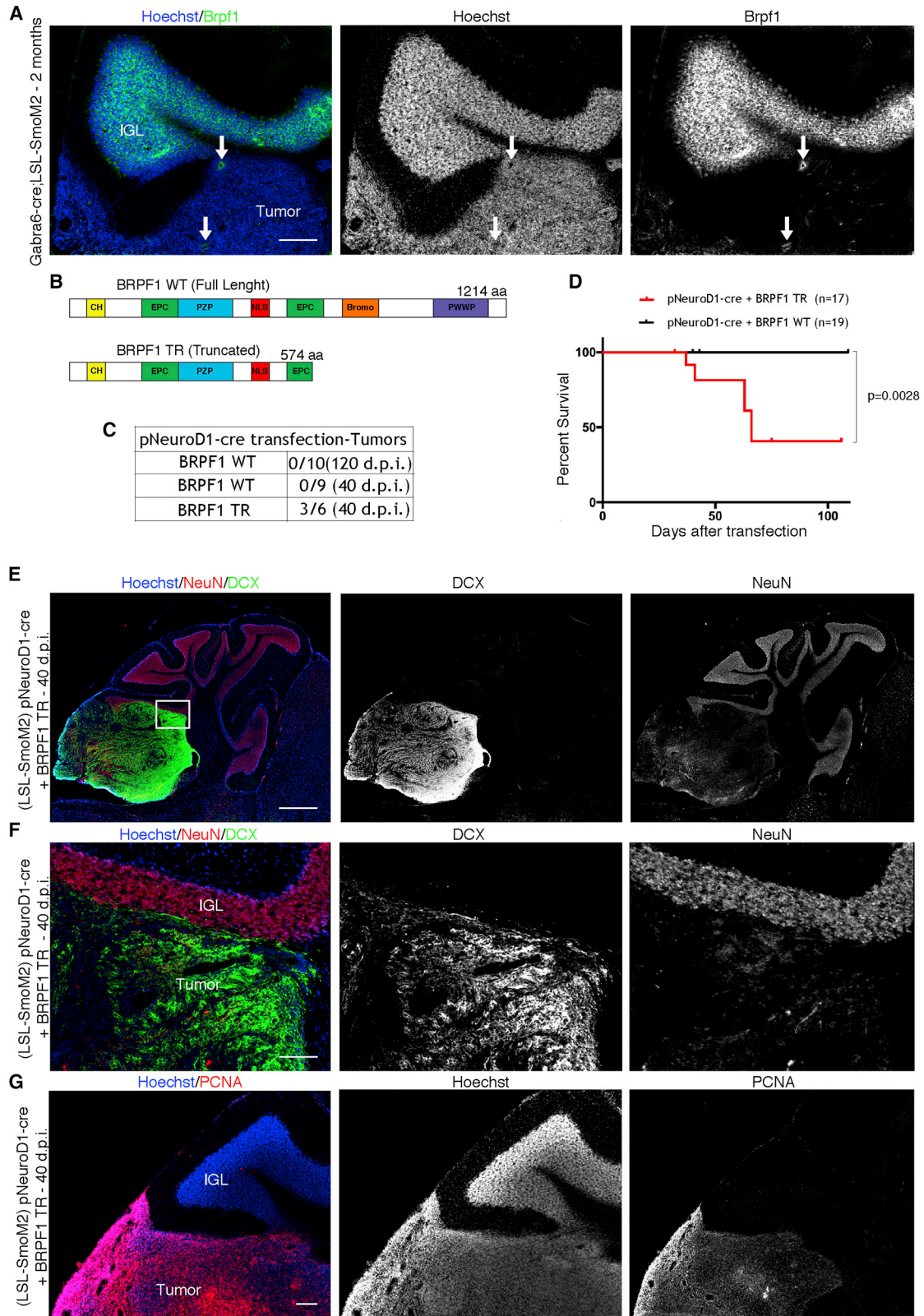
Mutant BRPF1 Promotes Adult Shh MB Formation

Looking for a molecular mechanism by which SmoM2 induces neuron dedifferentiation, we exploited already published data of human SHH MB exome sequencing. Interestingly, recurrent mutated genes have been identified in adult SHH MBs that were absent or very rare in pediatric SHH MBs, such as BRPF1, KIAA0182, TCF4, CREBBP, NEB, LRP1B, PIK3CA, FBXW7, KDM3B, XPO1, PRKAR1A, and PDE4D (Kool et al., 2014; Merk et al., 2018). For instance, nonsense and frameshift BRPF1 mutations have been found to be associated with SMO

mutations and absent in pediatric and adolescent SHH MBs (samples ID: AdRep_MB107, MB101, and MB143). The presence of a premature stop codon could generate truncated forms of BRPF1 proteins lacking several domains. Brpf1 has been previously shown to be expressed in granule neurons and Purkinje cells in newborn mice (You et al., 2014) and we found that Brpf1 is expressed in mouse cerebellum in P7 and 4-week-old mice (Figures S5C and S5D). We also analyzed the expression of Brpf1 in adult brains and in *Gabra6-cre;LSL-SmoM2* tumors. As shown in Figure 4A, Brpf1 was found to be expressed in cerebellar IGL and in a few cells within *Gabra6-cre;LSL-SmoM2* MBs. This indicates that Brpf1 protein is expressed at low levels in these tumors. Based on the described association of BRPF1 and SMO mutations in adult SHH MB, we tested its function in tumor formation. We co-transfected pNeuroD1-cre with a plasmid that allows constitutive expression of WT BRPF1 in *LSL-SmoM2* mice (pPB-BRPF1 WT; Figure 4B). Notably, we detected no sign of tumor/dysplasia in any of the 19 mice injected with pNeuroD1-cre and pPB-BRPF1 WT (Figures 4C and S5E), suggesting that BRPF1 overexpression blocks SmoM2's ability to induce neuron dedifferentiation. To mimic the mutational background of a subset of human patients, we generated a truncated form of BRPF1 lacking the bromodomain and PWWP motif (Figure 4B). Interestingly, we observed tumor formation when we co-transfected this truncated form of human BRPF1 (pPB-BRPF1 TR; Figure 4C) and a significant decrease in mouse survival compared to BRPF1 WT transfection (Figure 4D). We observed MB formation in 50% of the transfected mice (three out of six; Figure 4C) and the tumors were DCX, Sox9, and PCNA positive (Figures 4E–4G, S5F, and S5G). These data indicate that truncated BRPF1, as found in patients, is able to induce adult SHH MB. Next, we performed an *ex vivo* assay to test if BRPF1 also has a role in neuron dedifferentiation. Cerebellar cells from P7 *LSL-SmoM2* mice were nucleofected with *phSyn1-cre* alone or together with pPB-BRPF1 WT. After 7 days of *ex vivo* culture, we detected several GFP/Sox9/NeuN triple-positive cells in cerebellar cells nucleofected with *phSyn1-cre* alone (Figures S5H and S5I), but fewer with co-overexpression of BRPF1 WT, suggesting that BRPF1 WT blocks neuron dedifferentiation. Moreover, in the same experimental setup Gli1 co-overexpression was able to rescue the repressive effect of BRPF1 WT, indicating that the Shh pathway and BRPF1 WT could have antagonistic roles in the dedifferentiation process. Interestingly, the nucleofection of *phSyn1-cre* and a plasmid-expressing truncated BRPF1 did not block neuron dedifferentiation but rather increased it compared to *phSyn1-cre* alone (Figure S5J). This suggests that truncated BRPF1

Figure 3. Transient Cre Recombinase Expression Promotes Dedifferentiation of Granule Neurons and Shh MB in *LSL-SmoM2* Mice

- (A) GFP and NeuN staining of brain sections of *LSL-SmoM2* mice, 4 d.p.i. at P21 with pNeuroD1-cre. The arrow points to GFP and NeuN positive cells.
 (B) Quantification of GFP and Sox9/Sox2/PCNA double-positive cells in *LSL-SmoM2* mice, 4 d.p.i. at P21 with pNeuroD1-cre (n = 3).
 (C) Hoechst staining of brain sections of *LSL-SmoM2* mice, 60 d.p.i. at P21 with pNeuroD1-cre.
 (D) PCNA and NeuN staining of brain sections of *LSL-SmoM2* mice, 60 d.p.i. at P21 with pNeuroD1-cre. The arrow points to a tumorigenic cell cluster within the IGL.
 (E) Hoechst and DCX staining of brain sections of *LSL-SmoM2* mice, 60 d.p.i. at P21 with pNeuroD1-cre. The arrow points to a tumorigenic cell cluster within the IGL.
 (F) Mice with abnormal PCNA⁺ cell clusters or tumors.
 Scale bars, 1 mm in (C) and 150 μ m in (A), (D), and (E). d.p.i. days post injection; IGL, internal granular layer; ML, molecular layer.



(legend on next page)

could have a dominant-negative effect in promoting neuron dedifferentiation. Notably, *Gli1/2* knockdown was able to completely block *SmoM2* and truncated *BRPF1* functions, suggesting that they require *Gli1/2* expression to induce neuron dedifferentiation. Finally, to prove that neurons of adult mice can also give rise to adult *Shh* MBs, we transfected adult *LSL-SmoM2* animals (2 months old) with *phSyn1-cre* and *pPB-BRPF1 TR* (truncated *BRPF1*) plasmids. We obtained MB formation in three mice out of five (Figures 5A–5E) containing cancer cells positive for GFP, PCNA, and DCX. Furthermore, Kaplan-Meier survival analysis showed that less than 50% of the mice survived 100 days after transfection (Figure 5F). As previously shown in Figures S5A and S5B, *phSyn1-cre* transfection alone induced dedifferentiation of granule neurons, but did not lead to MB formation. This confirms that the *Shh* pathway and *BRPF1* functions should be altered together in adult mice during adult *Shh* MB tumorigenesis. Notably, we did not obtain *Shh* MB ($n = 11$) transfecting truncated *BRPF1* alone in 2-month-old CD1 mice (data not shown). To better characterize the *BRPF1*-induced MB, we performed gene expression profiling of single *phSyn1-cre+BRPF1 TR* and *pNeuroD1-cre+BRPF1 TR* tumors (Mouse *BRPF1*). Interestingly, the activation level of the *Shh* signaling pathway in the *SmoM2+BRPF1 TR* induced tumors was similar to human adult SHH MBs (Figure 5G). To evaluate if *phSyn1-cre+BRPF1 TR* and *pNeuroD1-cre+BRPF1 TR* tumors mimic human adult SHH MBs, we further compared their gene expression profiles with mouse and human MB samples. Based on the genes reported in Al-Halabi et al. (2011) as differentially expressed in human adult versus human infant SHH MB, *pNeuroD1-cre+BRPF1 TR* and *phSyn1-cre+BRPF1 TR* mouse models showed results similar to those for human adult SHH MB (Figure 5H). *Gabra6-cre;LSL-SmoM2* mice (one out of five samples) showed limited similarity to human adult SHH MB, while no similarity was observed for *Math1-cre;LSL-SmoM2* mice (GEO: GSE11859). These data suggest that *BRPF1 TR* and *SmoM2* co-overexpression in adult granule neurons gives rise to mouse tumors with a gene expression profile resembling human adult SHH MB. On the other hand, the tumors obtained from granule neuron progenitors are more similar to human infant SHH MB (*Math1-cre;LSL-SmoM2* mice; GEO: GSE11859). In addition, we performed immunofluorescence for p-AKT and p-S6 and the results have already been shown to be co-markers only for human adult SHH MB (Kool et al., 2014). In fact, few human infant SHH MBs are marked by p-AKT and p-S6 and always in a mutually exclusive way. The tumors generated upon transfection of *pNeuroD1-cre+BRPF1 TR* and *phSyn1-cre+BRPF1 TR* in *LSL-SmoM2*

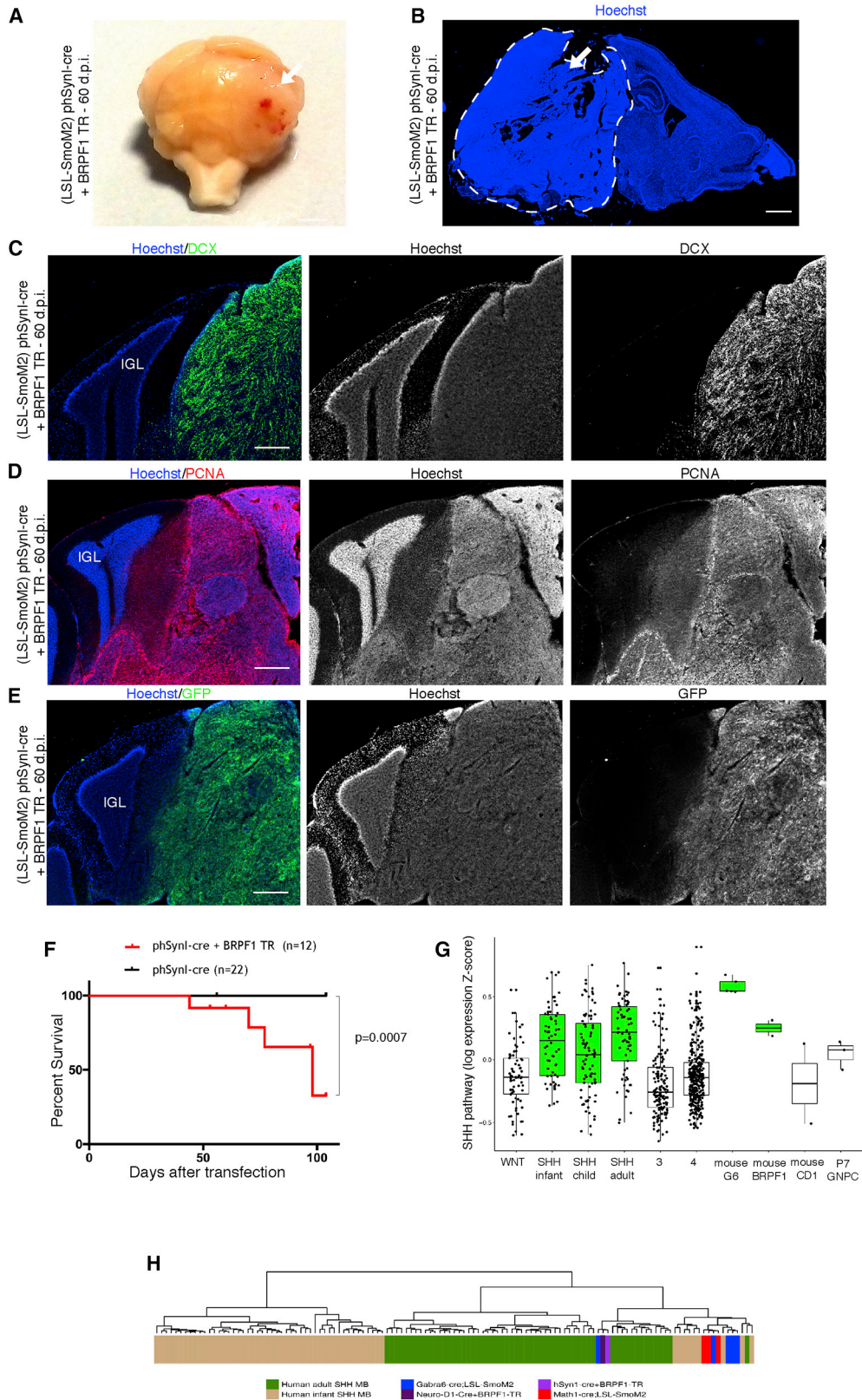
showed both p-AKT and p-S6, similar to human adult patients (Figures S5K–S5N; data not shown), while *Math1-creER;LSL-SmoM2* mice present only p-S6 (Figures S5O–S5R). Taken together, these data suggest that our mouse models resemble human adult SHH MB. To validate the cooperativity of *SmoM2* and truncated *BRPF1* in inducing adult *Shh* MB, we expressed in adult mice an inducible *cre* recombinase under the control of the *Etv1* promoter in postmitotic neurons (Schüller et al., 2006; Taniguchi et al., 2011). We transfected *Etv1-creER;LSL-SmoM2* mice with *pPB-BRPF1 TR* at P90 and then we induced the recombination with tamoxifen ($n = 9$). Notably, only one mouse developed MB (Figures S5S and S5T) and aberrant small clusters of cells were observed in two other mice (data not shown). We also tested the specificity of *Etv1-creER* recombination, transfecting *Etv1cre-ER;LSL-SmoM2* mice at P90 with *pPB-LSL-tdTomato*. In these animals, we did not detect any *tdTomato* and *Sox9/Sox2/PCNA/pH3* double-positive cells (Figure S5U). This confirms the role of *SmoM2* and truncated *BRPF1* in promoting MB formation from postmitotic neurons in adult mice. Finally, we assessed *BRPF1* expression in human adult SHH MBs derived from six different patients. In all of the tumors (Figures S5V and S5W; data not shown) we observed few *BRPF1*-positive cells within the PCNA-positive tumor cells, confirming that *BRPF1* protein is downregulated in human adult SHH MBs.

SmoM2 Expression in Granule Neurons Promotes Widespread Chromatin Plasticity

Considering that dedifferentiation of postmitotic cells requires overcoming those epigenetic barriers that are established to maintain cell identity (Fagnocchi et al., 2018; Poli et al., 2018), we investigated whether *SmoM2* expression in granule neurons was sufficient to alter the chromatin state. To this end, we profiled changes in chromatin accessibility by ATAC-seq in P14 cerebella of *Gabra6-cre;LSL-SmoM2* and *Gabra6-cre* control mice. ATAC-seq analyses defined approximately 130,000 open chromatin regions which were equally enriched at promoters (transcription start sites; TSSs), introns, and intergenic sites, independently from the genetic background (Figure 6A). Although most of the peaks were shared between the analyzed samples, we retrieved 4,029 and 6,025 open regions that were enriched in *Gabra6-cre* and *Gabra6-cre;LSL-SmoM2*, respectively (Figures 6B and S6A). Of importance, the differential enrichment of these regions was conserved among tissue samples obtained from independent mice (Figure 6C). The enriched regions for ATAC-seq signals showed a typical profile with narrow peaks, resembling nucleosome-depleted regions,

Figure 4. WT *BRPF1* Is Required to Block *Shh* MB Formation in *LSL-SmoM2* Mice

- (A) Hoechst and *Brpf1* staining of brain sections of 2-month-old *Gabra6-cre;LSL-SmoM2* mouse. The arrows point to *Brpf1*-positive cells.
 (B) Representation of human WT *BRPF1* and truncated *BRPF1*. Truncated *BRPF1* lacks the bromodomain and the PWWP motif. Bromo, bromodomain; CH, C2H2 zinc finger; EPC, enhancer of polycomb-like motif; NLS, nuclear localization signal; PWWP, Pro-Trp-Trp-Pro motif; PZP, PHD finger-zinc knuckle-PHD finger motif.
 (C) Mice with *Shh* MB after transfection at P21 with *pNeuroD1-cre* and *BRPF1 WT* or *BRPF1 TR*.
 (D) Kaplan-Meier survival curves of *LSL-SmoM2* mice transfected at P21 with *pNeuroD1-cre+BRPF1 WT* or *pNeuroD1-cre+BRPF1 TR*.
 (E and F) Hoechst, NeuN, and DCX staining of brain sections of *LSL-SmoM2* mouse, 40 d.p.i. at P21, with *pNeuroD1-cre+BRPF1 TR*. Square in (E) marks the region shown at higher magnification in (F).
 (G) Hoechst and PCNA staining of brain sections of *LSL-SmoM2* mouse; 40 d.p.i. at P21 with *pNeuroD1-cre+BRPF1 TR*.
 Scale bars, 200 μm in (A), 1 mm in (E), 500 μm in (G), and 150 μm in (F). IGL, internal granular layer. d.p.i. days post injection.



(legend on next page)

occupied by transcription factors (TFs) (Figure 6D). We confirmed that the ATAC-seq profiling on cerebella tissue enables the identification of *cis*-regulatory elements as we identified specific DNA-binding motifs enriched on the specific ATAC-seq peaks (Figure 6E). In *Gabra6-cre* samples we found binding motifs for neural-specific TFs and architectural proteins such as CTCF, which are normally enriched at sites of chromatin looping including enhancers (Rada-Iglesias et al., 2018). On *Gabra6-cre;LSL-SmoM2* ATAC-seq peaks, we identified DNA-binding motifs of lineage-specifying TFs, which are expressed during cerebellum development, such as *Sox2* and *Math1* (Figures 6E and S6B). These data were corroborated by Gene Ontology analysis on the genes annotated on specific ATAC-seq peaks highlighting the enrichment of specific signatures associated with stem-cell-like features and cancer pathways in *Gabra6-cre;LSL-SmoM2* (Figures 6F and S6C). This pattern was further confirmed by comparing the identified chromatin open regions with those that specified distinct stages of developing cerebellum (Frank et al., 2015). By quantifying the ATAC-seq signals on the previously identified chromatin accessible sites enriched at P14 and P60 (compared to P7) of developing cerebellum, we determined decreases in chromatin accessibility in *Gabra6-cre;LSL-SmoM2*, respect to *Gabra6-cre* (Figures 6G, S6D, and S6E). In sum, these results showed that activation of *SmoM2* in granule neurons induced changes in chromatin accessibility at *cis*-regulatory elements. These data suggest an increment of chromatin plasticity by means of favoring diversity in the chromatin contexts, priming for the activation of progenitor-associated transcriptional programs.

Truncated *Brpf1* Expression Elicits Chromatin Plasticity by Activating Super-Enhancers

As we showed that upon *SmoM2* activation the truncated BRPF1 protein induced MB in adult mice and considering its presumed function in chromatin regulation (Yan et al., 2017), we investigated whether it could favor tumorigenesis by promoting chromatin plasticity and neuronal dedifferentiation. To this end, we profiled the chromatin accessibility changes occurring in postmitotic neurons, in response to *SmoM2* activation alone or in cooperation with truncated BRPF1. We took advantage of the human neuroepithelial-like stem cells AF22, that have a gene expression pattern resembling hindbrain fate and committed to generate postmitotic neurons *in vitro* (Falk et al., 2012; Taylor et al., 2013) (Figure S6F). Indeed, quantitative real-time PCR analysis showed that differentiated AF22 cells expressed high levels of *ZIC1* gene, a specific

marker for cerebellar granule neurons (Aruga et al., 1998) (Figure S6G). To resemble the scenario already analyzed in mouse, we nucleofected AF22 with pPB-hSyn1-creER as control (Ctrl), and with pPB-hSyn1-creER+pPB-LSL-SmoM2 (*SmoM2*) or pPB-hSyn1-creER+pPB-LSL-SmoM2+pPB-LSL-BRPF1 TR (*SmoM2*+BRPF1 TR) to measure their cooperativity. Moreover, we tested the nucleofection with pPB-hSyn1-creER+pPB-LSL-BRPF1 TR (BRPF1 TR) to assess if truncated BRPF1 alone was sufficient per se to alter chromatin accessibility. Of importance, quantitative real-time PCR analysis confirmed that *SmoM2* overexpression increases *GLI1* mRNA levels in differentiated AF22 neurons (Figure S6H), as observed in *Gabra6-cre;LSL-SmoM2* mice (Figure S3A). Thereafter, we profiled changes in chromatin accessibility by ATAC-seq in AF22 neurons expressing the different combinations of *SmoM2* and BRPF1 (Figure 7A). ATAC-seq analyses defined comparable numbers of open chromatin regions that were similarly distributed within the genome (Figures 7A and S7A–S7C). At first we confirmed that *SmoM2* activation determined an increment in chromatin accessibility at specific *cis*-regulatory elements that were enriched for stem cells and *Sox*-family transcription factors (Figures S7D–S7G). Of importance, GSEA analysis confirmed that expression of *SmoM2* in human neurons negatively correlated with neuron chromatin accessible sites enriched at P14 and P60 (Figures S7H and S7I). Together, these results showed that we recapitulated the chromatin accessibility pattern found in mouse cerebella in response to *SmoM2*, also in human neurons. Thereafter, we investigated the contribution of truncated BRPF1 to alter the chromatin landscape. Differential analyses retrieved specific ATAC-seq regions enriched in BRPF1 TR and *SmoM2*+BRPF1 TR conditions (Figures 7B and 7C), which showed a profile resembling accessible *cis*-regulatory elements, similar to the ones detected in the mouse models (Figures 7D and S7J). GSEA analysis on the ATAC-seq signals showed that *SmoM2* activation correlated with cerebellum development, SHH pathways, and stem cell signatures, while we concurrently measured a decreased in chromatin accessibility on those regions associated with genes related to mature neuron functions (Figure 7E). These analyses indicate that, independent from the genetic background, *SmoM2* activation increased chromatin accessibility at stem/progenitor genes associated *loci* in neurons. Importantly, these features were further elicited by truncated BRPF1 (Figure S7K). Considering that cell fate specification and maintenance of cell identity are regulated by the activation of enhancers (also in human MBs)

Figure 5. Truncated BRPF1 Promotes Adult Shh MB

- (A) Image of *LSL-SmoM2* mouse; 60 d.p.i. at 2 months, with phSyn1-cre+BRPF1 TR. The arrow points to tumoral mass.
- (B) Hoechst staining of brain section of *LSL-SmoM2* mouse; 60 d.p.i. at 2 months, with phSyn1-cre+BRPF1 TR. The dashed lines and arrow in (B) mark the tumor.
- (C–E) Hoechst, DCX (C), PCNA (D), and GFP (E) staining of brain sections of *LSL-SmoM2* mouse; 60 d.p.i. at 2 months, with phSyn1-cre+BRPF1 TR.
- (F) Kaplan-Meier survival curves of *LSL-SmoM2* mice transfected at 2 months with either phSyn1-cre or phSyn1-cre+BRPF1 TR. Scale bars, 2 mm in (A), 1 mm in (B), and 500 μ m in (C)–(E).
- (G) Boxplots of the median values of the SHH pathway for the human samples (GEO: GSE85217) and our samples. BRPF1, 40 d.p.i. pNeuroD1-cre+BRPF1 TR and 60 d.p.i. phSyn1-cre+BRPF1 TR. *CD1*, normal cerebellum tissue. 3, group 3; 4, group 4; G6, *Gabra6-cre;LSL-SmoM2*; P7 GNPC, P7 granule neuron progenitor cells; SHH, SHH subgroup; WNT, WNT subgroup.
- (H) Hierarchical clustering of different Shh MB mouse models and human adult/infant SHH MB data on both samples distances and samples gene expression profiles using 108 differentially expressed genes in human adult versus human infant SHH MB.
- d.p.i., days post injection; IGL, internal granular layer.

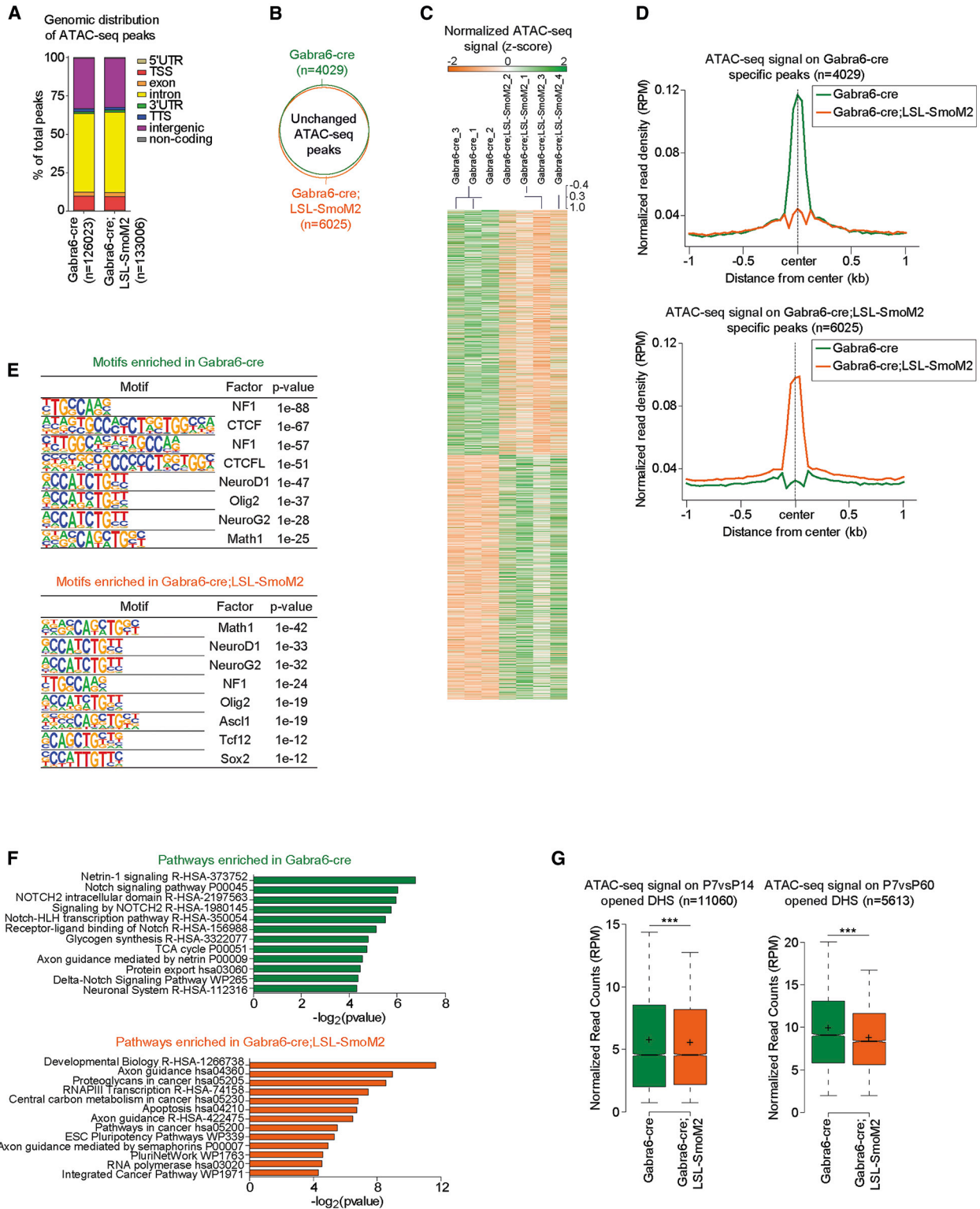


Figure 6. SmoM2 Expression in Granule Neurons Favors Widespread Chromatin Plasticity and Activation of Stem/Progenitor-Associated Genes

(A) Boxplots showing the genomic distribution of ATAC-seq peaks, with respect to transcription start sites (TSSs), transcription termination sites (TTSs), 5'UTR, 3'UTR, exons, introns, intergenic regions, and non-coding genes.

(legend continued on next page)

(Lin et al., 2016), we asked whether the measured changes in chromatin accessibility were associated with enhancers modulation. ATAC-seq analysis on annotated human enhancers (Shen et al., 2014) showed that, while BRPF1 TR per se did not alter chromatin accessibility (Figure S7L), its co-expression with SmoM2 induced an increment of chromatin opening (Figure 7F). Given the relative spread pattern of the retrieved ATAC-seq signal distribution on these enhancers (Figure 7F), we asked whether the expression of SmoM2+BRPF1 TR could augment chromatin accessibility to lineage-specifying clustered enhancers, referred as super-enhancers (Lovén et al., 2013). By clustering ATAC-seq peaks, which reside in proximity in a given locus, we identified super-enhancers in all the analyzed conditions (Figures 7G and S7M). Independently from the genetic background, we noticed that the expression of BRPF1 TR increased the number of unique super-enhancers (Figures 7G and S7M). Of importance, in the SmoM2+BRPF1 TR neurons we defined 241 clusters of enhancers with an average size spanning over 33 kb (Figures 7G and 7H). By measuring the relative enrichment of the ATAC-seq signal, we depicted a clear increase in chromatin accessibility associated with the concomitant expression of SmoM2 and BRPF1 TR (Figure 7H). Moreover, we found that the identified super-enhancers were linked to key genes involved in cerebellum development (GBX2 and LMX1B) (Wasarman et al., 1997; Guo et al., 2007) and chromatin remodeling (KDM6B, KDM4B, KMT2C). Gene Ontology analyses confirmed that the SmoM2+BRPF1 TR super-enhancers were specifically associated with chromatin-modifying enzymes, but also with base-excision repair, suggesting a possible involvement of DNA damage response (Figures 7I and S7N). Finally, to assess whether the identified *cis*-regulatory elements in neurons expressing SmoM2+BRPF1 TR resembled specific chromatin features of human SHH MBs, we measured changes of chromatin accessibility on the previously annotated SHH MB enhancers (Lin et al., 2016). This analysis showed that BRPF1 TR expression induced an increment of chromatin opening on SHH enhancers (Figure 7J) and also on SHH associates super-enhancers (Figure 7K). Of importance, the contribution of BRPF1 TR to increased chromatin accessibility was specifically dependent on SmoM2 activation, as the same changes were not detected in truncated BRPF1 alone (Figures S7O and S7P). Taken together, these data showed that truncated BRPF1 cooperates with SmoM2 by promoting chromatin accessibility at clustered enhancers that are linked to genes involved in chromatin remodeling.

DISCUSSION

Cancer is viewed as an evolutionary conserved process that results from the accumulation of somatic mutations in the progeny of a normal cell and it is a common opinion that the cells of origin should possess a proliferative capacity (Blainpain, 2013; Visvader, 2011). Interestingly, few groups have attempted to induce cancer from neurons using full KO mice for cell-cycle regulators or by genetic modification of mice and *Drosophila melanogaster* although rare targeting of progenitors cannot be excluded (Alcantara Llaguno and Parada, 2016; Arlotta and Berninger, 2014). Notably, adult SHH MB arises when progenitors are no longer present and for this reason postmitotic neurons could represent the cell of origin. In the present work we showed that constitutive activation of Shh pathway induced by SmoM2 mutation, specifically in mouse cerebellar granule neurons, promotes the expression of progenitor- and proliferation-associated markers, enabling postmitotic neurons to re-enter in the cell cycle and give rise to Shh MB. Interestingly, activation of the Shh pathway in other CNS neurons does not induce cancer, suggesting that granule neurons have defined intrinsic characteristics that allow the dedifferentiation process. Notably, the deletion of oncosuppressor Ptch1 in granule neurons was not able to recapitulate Shh MB development, as observed with the overexpression of SmoM2. Indeed, Ptch1 deletion led to a lower induction of Shh signaling as compared to SmoM2 constitutive activation, suggesting that other mutational hits could be required. In line with our observations, it has been recently found that tumor suppressors deletion in neurons (cerebral cortex) leads to extended cell division but no glioma formation (Alcantara Llaguno et al., 2019). On the other hand, we performed oncogene overexpression (smoothed gain of function) and we checked for co-mutated genes in the adult SHH MB. Several adult SHH MB patients present truncated mutations of the chromatin reader BRPF1 that are often associated with SMO mutations and absent in pediatric and adolescent patients (Kool et al., 2014). To mimic the mutational background of a subset of human patients, a truncated form of BRPF1 was overexpressed together with SmoM2, exploiting the neuronal promoters NeuroD1 and hSyn1. Truncated BRPF1 and SmoM2 co-overexpression led to neuronal dedifferentiation and Shh MB in adult mice. Our data show that a second mutational hit is essential to faithfully recapitulate the adult condition, because constitutive activation of the Shh pathway alone rarely induced MB; otherwise, the co-overexpression of SmoM2 and truncated BRPF1 in adult mice is

(B) Venn diagram showing the overlap between ATAC-seq peaks in *Gabra6-cre* and *Gabra6-cre;LSL-SmoM2* cells.

(C) Heatmap representing the normalized ATAC-seq signal (Z score) on the top 2,000 most differentially enriched peaks in either *Gabra6-cre* or *Gabra6-cre;LSL-SmoM2* cells.

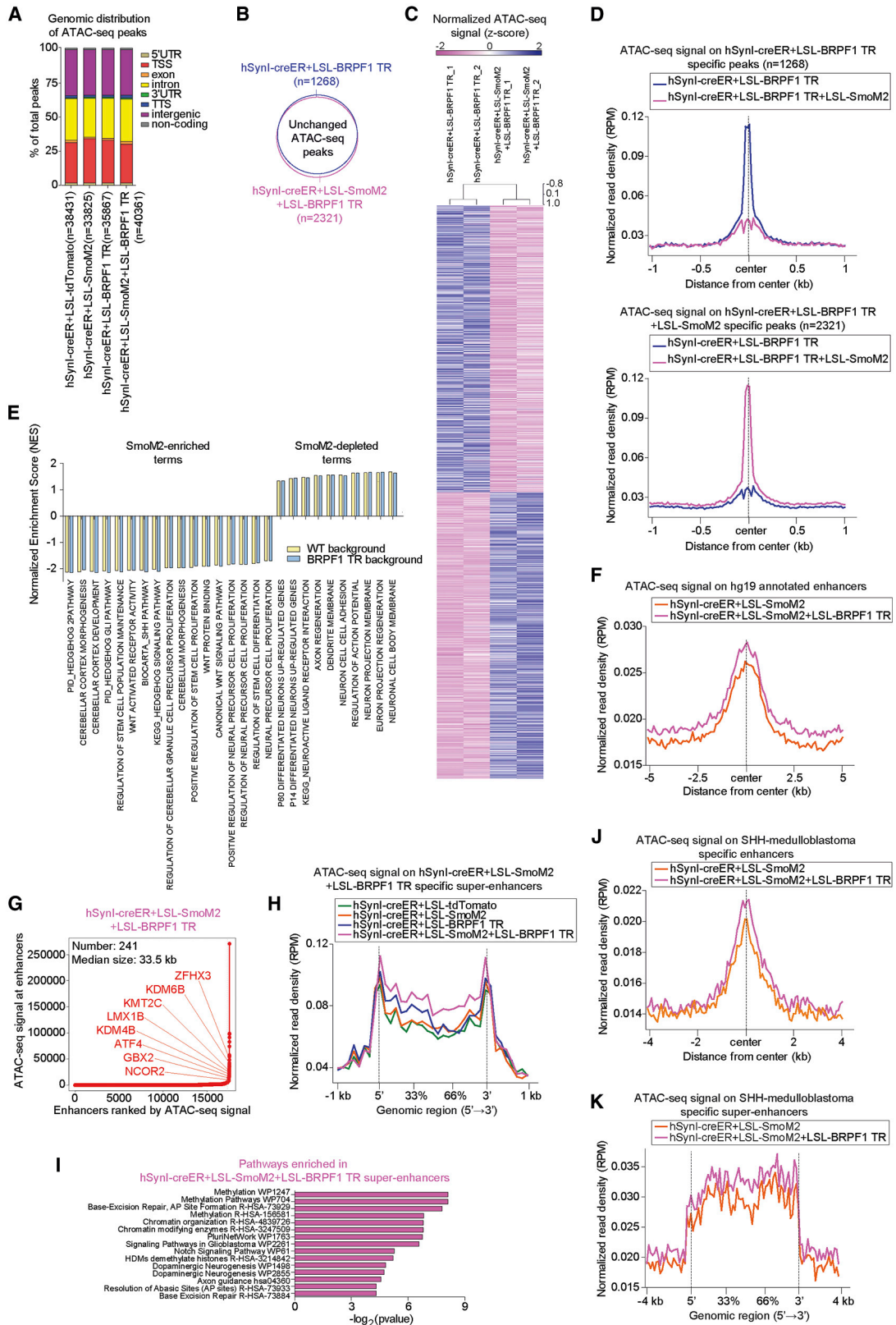
(D) Average tag density plot of the normalized (RPM) ATAC-seq signal on the differential peaks, enriched in *Gabra6-cre* (top panel) or *Gabra6-cre;LSL-SmoM2* (bottom panel) cells.

(E) Motif enrichment analysis on the specific ATAC-seq peaks in *Gabra6-cre* (left panel) or *Gabra6-cre;LSL-SmoM2* (right panel) cells.

(F) Gene Ontology analysis on the genes annotated to specific ATAC-seq peaks in *Gabra6-cre* (top panel) or *Gabra6-cre;LSL-SmoM2* (bottom panel) cells. Pathways from Reactome, Panther, WikiPathways, and KEGG databases were analyzed.

(G) Boxplots showing the normalized read counts of ATAC-seq signals in *Gabra6-cre* and *Gabra6-cre;LSL-SmoM2* cells, on previously reported DNase hypersensitive sites (DHSs), resulting in more accessibility in P14 (left) or P60 (right) cerebella, when compared to P7 cerebella.

****p* < 0.001, as assessed by a two-tailed, unpaired Student's *t* test. P14 *Gabra6-cre* (*n* = 3) and *Gabra6-cre;LSL-SmoM2* (*n* = 4) cerebella.



(legend on next page)

able to promote adult Shh MB development. Gene expression analysis confirmed the similarity between human adult SHH MBs and the tumors originated by truncated BRPF1 and SmoM2 co-overexpression. Notably, only the oldest Gaba6-associated MB resembles the transcriptomic level of human adult SHH MB, probably due to its late onset. In addition, tumors generated upon transfection of truncated BRPF1 exhibited p-Akt and p-S6 markers that are exclusively associated to human adult SHH MB patients. Finally, ATAC-seq analysis revealed that SmoM2 overexpression reshaped the chromatin structure of granule neurons, enriching the number of open chromatin regions associated with stem/progenitor-like genes. Moreover, it pointed out a synergistic mechanism between SmoM2 and truncated BRPF1 in modifying the chromatin accessibility of postmitotic neurons, increasing the number of super-enhancers associated with chromatin organization/modification genes. Overall, the performed experiments demonstrated the role of truncated BRPF1 in altering the chromatin landscape of *cis*-regulatory elements. We believe that these findings could open new roads toward understanding the link between chromatin reshaping and cell dedifferentiation occurring in human patients and leading to tumor formation. Our work establishes a mouse model for human adult SHH MB, showing that postmitotic granule neurons own the capability to re-enter in the cell cycle and give rise to tumors upon the proper oncogenic mutational hit. Remarkably, we uncover that BRPF1 might be one of the key genes involved in adult Shh MB formation and its truncated form could be relevant to mimicking neuronal dedifferentiation and adult Shh MB development.

STAR★METHODS

Detailed methods are provided in the online version of this paper and include the following:

- KEY RESOURCES TABLE
- LEAD CONTACT AND MATERIALS AVAILABILITY

- EXPERIMENTAL MODEL AND SUBJECT DETAILS
 - Mice
 - Human Adult SHH Medulloblastoma Samples
 - Cell Lines and Primary Cell Cultures
- METHOD DETAILS
 - Plasmids
 - *In Vivo* Transfection of Granule Neurons
 - Transplantation of Tumor Cells in Nude Mice
 - Histopathological Evaluation
 - Immunofluorescence
 - EdU Staining
 - Imaging
 - Cell Quantification
 - RNA Isolation and Real-Time PCR Analysis
 - Survival Analysis
 - ATAC-Seq
 - Microarray Analysis
- QUANTIFICATION AND STATISTICAL ANALYSIS
 - Statistical Analysis
- DATA AND CODE AVAILABILITY

SUPPLEMENTAL INFORMATION

Supplemental Information can be found online at <https://doi.org/10.1016/j.celrep.2019.11.046>.

ACKNOWLEDGMENTS

We thank Dr. Pierre Vanderhaeghen, Alessandro Quattrone, Alessia Soldano, Francesco Antonica, Cedric Blanpain, Alberto Inga, Luciano Conti, Yuri Bozzi, Simona Casarosa, Bassem Hassan, and Andrea Lunardi for helpful discussions and advice. We thank Sergio Robbiati (MOF facility) and Veronica De Sanctis, Roberto Bertorelli, and Paola Fossan (NGS facility). We thank Dr. William Wisden (Imperial College London) for providing us with Gaba6-cre mice and Dr. Jacques Cote (Laval University Cancer Research Center) for providing us with human BRPF1 cDNA. This work was funded by a grant from the Giovanni Armenise-Harvard Foundation, United States (Career Development Award 2016, to L.T.) and My First AIRC Grant, Italy (Project Code: 19921 to L.T.).

Figure 7. Truncated Brpf1 Potentiates the Effect of SmoM2, by Reprogramming the Super-Enhancers Landscape

- (A) Boxplots showing the genomic distribution of ATAC-seq peaks, with respect to TSSs, TTSSs, 5'UTR, 3'UTR, exons, introns, intergenic regions, and non-coding genes, in the indicated cell lines.
- (B) Venn diagram showing the overlap between ATAC-seq peaks in hSyn1-creER+LSL-BRPF1 TR and hSyn1-creER+LSL-SmoM2+LSL-BRPF1 TR cells.
- (C) Heatmap representing the normalized ATAC-seq signal (Z score) on the top 2,000 most differentially enriched peaks in either hSyn1-creER+LSL-BRPF1 TR or hSyn1-creER+LSL-SmoM2+LSL-BRPF1 TR cells.
- (D) Average tag density plot of the normalized (RPM) ATAC-seq signal on the differential peaks, enriched either in hSyn1-creER+LSL-BRPF1 TR (top panel) or hSyn1-creER+LSL-SmoM2+LSL-BRPF1 TR (bottom panel) cells.
- (E) GSEA of indicated gene lists, in hSyn1-creER+LSL-BRPF1 TR versus hSyn1-creER+LSL-SmoM2+LSL-BRPF1 TR cells. All gene lists are enriched with a statistical $p < 0.05$.
- (F) Average tag density plot of the normalized (RPM) ATAC-seq signals in hSyn1-creER+LSL-SmoM2 and hSyn1-creER+LSL-SmoM2+LSL-BRPF1 TR cells, on annotated enhancer regions of human genome hg19/GRCh37.
- (G) Distribution of the ATAC-seq signal across hSyn1-creER+LSL-SmoM2+LSL-BRPF1 TR enhancers, showing the presence of 241 super-enhancers. Representative super-enhancers are highlighted along with their associated genes.
- (H) Average tag density plot of the normalized (RPM) ATAC-seq signals in indicated cell lines, hSyn1-creER+LSL-SmoM2+LSL-BRPF1 TR-specific super-enhancers.
- (I) Gene Ontology analysis on the genes associated to hSyn1-creER+LSL-SmoM2+LSL-BRPF1 TR-specific super-enhancers. Pathways from Reactome, Panther, WikiPathways, and KEGG databases were analyzed.
- (J and K) Average tag density plot of the normalized (RPM) ATAC-seq signals in hSyn1-creER+LSL-SmoM2 and hSyn1-creER+LSL-SmoM2+LSL-BRPF1 TR cells, on previously reported enhancers (J) and super-enhancers (K), which characterize the SHH MB. Analyses are performed on two biological replicates for each cell line.

AUTHOR CONTRIBUTIONS

G.A., C.B., R.R., M.A., I.M., D.C., and F. Garilli performed all experiments. A.R. and S.P. performed the Bioinformatics analyses. L.F. and A.Z. performed and analyzed the ATAC-seq data. G.A. and L.T. designed and analyzed all experiments and wrote the manuscript. F. Gianni and F. Giangaspero performed histopathological analysis of *Gabra6-cre;LSL-SmoM2* MB.

DECLARATION OF INTERESTS

The authors declare no competing interests.

Received: June 21, 2018

Revised: May 14, 2019

Accepted: November 12, 2019

Published: December 17, 2019

REFERENCES

- Ahlfeld, J., Favaro, R., Pagella, P., Kretzschmar, H.A., Nicolis, S., and Schüller, U. (2013). Sox2 requirement in sonic hedgehog-associated medulloblastoma. *Cancer Res.* *73*, 3796–3807.
- Ajjoka, I., Martins, R.A.P., Bayazitov, I.T., Donovan, S., Johnson, D.A., Frase, S., Cicero, S.A., Boyd, K., Zakharenko, S.S., and Dyer, M.A. (2007). Differentiated horizontal interneurons clonally expand to form metastatic retinoblastoma in mice. *Cell* *131*, 378–390.
- Alcantara Llaguno, S.R., and Parada, L.F. (2016). Cell of origin of glioma: biological and clinical implications. *Br. J. Cancer* *115*, 1445–1450.
- Alcantara Llaguno, S., Sun, D., Pedraza, A.M., Vera, E., Wang, Z., Burns, D.K., and Parada, L.F. (2019). Cell-of-origin susceptibility to glioblastoma formation declines with neural lineage restriction. *Nat. Neurosci.* *22*, 545–555.
- Al-Halabi, H., Nantel, A., Klekner, A., Guiot, M.C., Albrecht, S., Hauser, P., Garami, M., Bognar, L., Kavan, P., Gerges, N., et al. (2011). Preponderance of sonic hedgehog pathway activation characterizes adult medulloblastoma. *Acta Neuropathol.* *121*, 229–239.
- Aller, M.I., Jones, A., Merlo, D., Paterlini, M., Meyer, A.H., Amtmann, U., Brickley, S., Jolin, H.E., McKenzie, A.N.J., Monyer, H., et al. (2003). Cerebellar granule cell Cre recombinase expression. *Genesis* *36*, 97–103.
- Arlotta, P., and Berninger, B. (2014). Brains in metamorphosis: reprogramming cell identity within the central nervous system. *Curr. Opin. Neurobiol.* *27*, 208–214.
- Aruga, J., Minowa, O., Yaginuma, H., Kuno, J., Nagai, T., Noda, T., and Mikkoshiba, K. (1998). Mouse *Zic1* is involved in cerebellar development. *J. Neurosci.* *18*, 284–293.
- Benjamini, Y., and Hochberg, Y. (1995). Controlling the False Discovery Rate: A Practical and Powerful Approach to Multiple Testing. *J. R. Stat. Soc. Series B Stat. Methodol.* *57*, 289–300.
- Blanpain, C. (2013). Tracing the cellular origin of cancer. *Nat. Cell Biol.* *15*, 126–134.
- Bolger, A.M., Lohse, M., and Usadel, B. (2014). Trimmomatic: a flexible trimmer for Illumina sequence data. *Bioinformatics* *30*, 2114–2120.
- Chen, E.Y., Tan, C.M., Kou, Y., Duan, Q., Wang, Z., Meirelles, G.V., Clark, N.R., and Ma'ayan, A. (2013). Enrichr: interactive and collaborative HTML5 gene list enrichment analysis tool. *BMC Bioinformatics* *14*, 128.
- Cho, J.H., and Tsai, M.J. (2006). Preferential posterior cerebellum defect in *BETA2/NeuroD1* knockout mice is the result of differential expression of *BETA2/NeuroD1* along anterior-posterior axis. *Dev. Biol.* *290*, 125–138.
- Corces, M.R., Trevino, A.E., Hamilton, E.G., Greenside, P.G., Sinnott-Armstrong, N.A., Vesuna, S., Satpathy, A.T., Rubin, A.J., Montine, K.S., Wu, B., et al. (2017). An improved ATAC-seq protocol reduces background and enables interrogation of frozen tissues. *Nat. Methods* *14*, 959–962.
- Dai, M., Wang, P., Boyd, A.D., Kostov, G., Athey, B., Jones, E.G., Bunney, W.E., Myers, R.M., Speed, T.P., Akil, H., et al. (2005). Evolving gene/transcript definitions significantly alter the interpretation of GeneChip data. *Nucleic Acids Res.* *33*, e175.
- Deneris, E.S., and Hobert, O. (2014). Maintenance of postmitotic neuronal cell identity. *Nat. Neurosci.* *17*, 899–907.
- Eijssen, L.M.T., Jaillard, M., Adriaens, M.E., Gaj, S., de Groot, P.J., Müller, M., and Evelo, C.T. (2013). User-friendly solutions for microarray quality control and pre-processing on. *Nucleic Acids Res.* *41*, W71–W76. ArrayAnalysis.org.
- Ellison, D.W., Dalton, J., Kocak, M., Nicholson, S.L., Fraga, C., Neale, G., Kenney, A.M., Brat, D.J., Perry, A., Yong, W.H., et al. (2011). Medulloblastoma: clinicopathological correlates of SHH, WNT, and non-SHH/WNT molecular subgroups. *Acta Neuropathol.* *121*, 381–396.
- Fagnocchi, L., Poli, V., and Zippo, A. (2018). Enhancer reprogramming in tumor progression: a new route towards cancer cell plasticity. *Cell. Mol. Life Sci.* *75*, 2537–2555.
- Falk, A., Koch, P., Kesavan, J., Takashima, Y., Ladewig, J., Alexander, M., Wiskow, O., Tailor, J., Trotter, M., Pollard, S., et al. (2012). Capture of neuroepithelial-like stem cells from pluripotent stem cells provides a versatile system for in vitro production of human neurons. *PLoS ONE* *7*, e29597.
- Frank, C.L., Liu, F., Wijayatunge, R., Song, L., Biegler, M.T., Yang, M.G., Vockley, C.M., Safi, A., Gersbach, C.A., Crawford, G.E., and West, A.E. (2015). Regulation of chromatin accessibility and *Zic* binding at enhancers in the developing cerebellum. *Nat. Neurosci.* *18*, 647–656.
- Friedmann-Morvinski, D., Bushong, E.A., Ke, E., Soda, Y., Marumoto, T., Singer, O., Ellisman, M.H., and Verma, I.M. (2012). Dedifferentiation of neurons and astrocytes by oncogenes can induce gliomas in mice. *Science* *338*, 1080–1084.
- Gautier, L., Cope, L., Bolstad, B.M., and Irizarry, R.A. (2004). affy-analysis of Affymetrix GeneChip data at the probe level. *Bioinformatics* *20*, 307–315.
- Guerrier, S., Coutinho-Budd, J., Sassa, T., Gresset, A., Jordan, N.V., Chen, K., Jin, W.L., Frost, A., and Polleux, F. (2009). The F-BAR domain of srGAP2 induces membrane protrusions required for neuronal migration and morphogenesis. *Cell* *138*, 990–1004.
- Guo, C., Qiu, H.Y., Huang, Y., Chen, H., Yang, R.Q., Chen, S.D., Johnson, R.L., Chen, Z.-F., and Ding, Y.Q. (2007). *Lmx1b* is essential for *Fgf8* and *Wnt1* expression in the isthmic organizer during tectum and cerebellum development in mice. *Development* *134*, 317–325.
- Heinz, S., Benner, C., Spann, N., Bertolino, E., Lin, Y.C., Laslo, P., Cheng, J.X., Murre, C., Singh, H., and Glass, C.K. (2010). Simple combinations of lineage-determining transcription factors prime cis-regulatory elements required for macrophage and B cell identities. *Mol. Cell* *38*, 576–589.
- Huang, W., Sherman, B.T., and Lempicki, R.A. (2009). Systematic and integrative analysis of large gene lists using DAVID bioinformatics resources. *Nat. Protoc.* *4*, 44–57.
- Irizarry, R.A., Bolstad, B.M., Collin, F., Cope, L.M., Hobbs, B., and Speed, T.P. (2003). Summaries of Affymetrix GeneChip probe level data. *Nucleic Acids Res.* *31*, e15.
- Johnson, W.E., Li, C., and Rabinovic, A. (2007). Adjusting batch effects in microarray expression data using empirical Bayes methods. *Biostatistics* *8*, 118–127.
- Kool, M., Jones, D.T.W., Jäger, N., Northcott, P.A., Pugh, T.J., Hovestadt, V., Piro, R.M., Esparza, L.A., Markant, S.L., Remke, M., et al.; ICGC PedBrain Tumor Project (2014). Genome sequencing of SHH medulloblastoma predicts genotype-related response to smoothed inhibition. *Cancer Cell* *25*, 393–405.
- Kügler, S., Kilic, E., and Bähr, M. (2003). Human synapsin 1 gene promoter confers highly neuron-specific long-term transgene expression from an adenoviral vector in the adult rat brain depending on the transduced area. *Gene Ther.* *10*, 337–347.
- Kuleshov, M.V., Jones, M.R., Rouillard, A.D., Fernandez, N.F., Duan, Q., Wang, Z., Koplev, S., Jenkins, S.L., Jagodnik, K.M., Lachmann, A., et al.

- (2016). Enrichr: a comprehensive gene set enrichment analysis web server 2016 update. *Nucleic Acids Res.* *44* (W1), W90–W97.
- Langmead, B., and Salzberg, S.L. (2012). Fast gapped-read alignment with Bowtie 2. *Nat. Methods* *9*, 357–359.
- Larsimont, J.C., Youssef, K.K., Sánchez-Danés, A., Sukumaran, V., Defrance, M., Delatte, B., Liagre, M., Baatsen, P., Marine, J.C., Lippens, S., et al. (2015). Sox9 Controls Self-Renewal of Oncogene Targeted Cells and Links Tumor Initiation and Invasion. *Cell Stem Cell* *17*, 60–73.
- Larson, D.R., Zenklusen, D., Wu, B., Chao, J.A., and Singer, R.H. (2011). Real-time observation of transcription initiation and elongation on an endogenous yeast gene. *Science* *332*, 475–478.
- Li, H., Handsaker, B., Wysoker, A., Fennell, T., Ruan, J., Homer, N., Marth, G., Abecasis, G., and Durbin, R.; 1000 Genome Project Data Processing Subgroup (2009). The Sequence Alignment/Map format and SAMtools. *Bioinformatics* *25*, 2078–2079.
- Lin, C.Y., Erkek, S., Tong, Y., Yin, L., Federation, A.J., Zapatka, M., Haldipur, P., Kawachi, D., Risch, T., Warnatz, H.J., et al. (2016). Active medulloblastoma enhancers reveal subgroup-specific cellular origins. *Nature* *530*, 57–62.
- Lovén, J., Hoke, H.A., Lin, C.Y., Lau, A., Orlando, D.A., Vakoc, C.R., Bradner, J.E., Lee, T.I., and Young, R.A. (2013). Selective inhibition of tumor oncogenes by disruption of super-enhancers. *Cell* *153*, 320–334.
- Madisen, L., Zwingman, T.A., Sunkin, S.M., Oh, S.W., Zariwala, H.A., Gu, H., Ng, L.L., Palmiter, R.D., Hawrylycz, M.J., Jones, A.R., et al. (2010). A robust and high-throughput Cre reporting and characterization system for the whole mouse brain. *Nat. Neurosci.* *13*, 133–140.
- Martz, C.A., Ottina, K.A., Singleton, K.R., Jasper, J.S., Wardell, S.E., Peraza-Penton, A., Anderson, G.R., Winter, P.S., Wang, T., Alley, H.M., et al. (2014). Systematic identification of signaling pathways with potential to confer anti-cancer drug resistance. *Sci. Signal.* *7*, ra121.
- Marzban, H., Del Bigio, M.R., Alizadeh, J., Ghavami, S., Zachariah, R.M., and Rastegar, M. (2015). Cellular commitment in the developing cerebellum. *Front. Cell. Neurosci.* *8*, 450.
- McLean, C.Y., Bristor, D., Hiller, M., Clarke, S.L., Schaar, B.T., Lowe, C.B., Wenger, A.M., and Bejerano, G. (2010). GREAT improves functional interpretation of cis-regulatory regions. *Nat. Biotechnol.* *28*, 495–501.
- Merk, D.J., Ohli, J., Merk, N.D., Thatikonda, V., Morrissy, S., Schoof, M., Schmid, S.N., Harrison, L., Filser, S., Ahlfeld, J., et al. (2018). Opposing Effects of CREBBP Mutations Govern the Phenotype of Rubinstein-Taybi Syndrome and Adult SHH Medulloblastoma. *Dev. Cell* *44*, 709–724.e6.
- Nguyen, L., Besson, A., Roberts, J.M., and Guillemot, F. (2006). Coupling cell cycle exit, neuronal differentiation and migration in cortical neurogenesis. *Cell Cycle* *5*, 2314–2318.
- Northcott, P.A., Jones, D.T.W., Kool, M., Robinson, G.W., Gilbertson, R.J., Cho, Y.J., Pomeroy, S.L., Korshunov, A., Lichter, P., Taylor, M.D., and Pfister, S.M. (2012). Medulloblastomics: the end of the beginning. *Nat. Rev. Cancer* *12*, 818–834.
- Poli, V., Fagnocchi, L., Fasciani, A., Cherubini, A., Mazzoleni, S., Ferrillo, S., Miluzio, A., Gaudioso, G., Vaira, V., Turdo, A., et al. (2018). MYC-driven epigenetic reprogramming favors the onset of tumorigenesis by inducing a stem cell-like state. *Nat. Commun.* *9*, 1024.
- Quinlan, A.R., and Hall, I.M. (2010). BEDTools: a flexible suite of utilities for comparing genomic features. *Bioinformatics* *26*, 841–842.
- Rada-Iglesias, A., Grosveld, F.G., and Papantonis, A. (2018). Forces driving the three-dimensional folding of eukaryotic genomes. *Mol. Syst. Biol.* *14*, e8214.
- Ritchie, M.E., Phipson, B., Wu, D., Hu, Y., Law, C.W., Shi, W., and Smyth, G.K. (2015). limma powers differential expression analyses for RNA-sequencing and microarray studies. *Nucleic Acids Res.* *43*, e47.
- Rose, M.F., Ren, J., Ahmad, K.A., Chao, H.T., Klisch, T.J., Flora, A., Greer, J.J., and Zoghbi, H.Y. (2009). Math1 is essential for the development of hindbrain neurons critical for perinatal breathing. *Neuron* *64*, 341–354.
- Schüller, U., Kho, A.T., Zhao, Q., Ma, Q., and Rowitch, D.H. (2006). Cerebellar ‘transcriptome’ reveals cell-type and stage-specific expression during post-natal development and tumorigenesis. *Mol. Cell. Neurosci.* *33*, 247–259.
- Schüller, U., Heine, V.M., Mao, J., Kho, A.T., Dillon, A.K., Han, Y.G., Huillard, E., Sun, T., Ligon, A.H., Qian, Y., et al. (2008). Acquisition of granule neuron precursor identity is a critical determinant of progenitor cell competence to form Shh-induced medulloblastoma. *Cancer Cell* *14*, 123–134.
- Sergushichev, A.A. (2016). An algorithm for fast preranked gene set enrichment analysis using cumulative statistic calculation. *bioRxiv*. <https://doi.org/10.1101/060012>.
- Shen, L., Shao, N., Liu, X., and Nestler, E. (2014). ngs.plot: Quick mining and visualization of next-generation sequencing data by integrating genomic databases. *BMC Genomics* *15*, 284.
- Southall, T.D., Davidson, C.M., Miller, C., Carr, A., and Brand, A.H. (2014). Dedifferentiation of neurons precedes tumor formation in *Lola* mutants. *Dev. Cell* *28*, 685–696.
- Subramanian, A., Tamayo, P., Mootha, V.K., Mukherjee, S., Ebert, B.L., Gillette, M.A., Paulovich, A., Pomeroy, S.L., Golub, T.R., Lander, E.S., and Mesirov, J.P. (2005). Gene set enrichment analysis: a knowledge-based approach for interpreting genome-wide expression profiles. *Proc. Natl. Acad. Sci. USA* *102*, 15545–15550.
- Sutter, R., Shakhova, O., Bhagat, H., Behesti, H., Sutter, C., Penkar, S., Santucione, A., Bernays, R., Heppner, F.L., Schüller, U., et al. (2010). Cerebellar stem cells act as medulloblastoma-initiating cells in a mouse model and a neural stem cell signature characterizes a subset of human medulloblastomas. *Oncogene* *29*, 1845–1856.
- Swartling, F.J., Savov, V., Persson, A.I., Chen, J., Hackett, C.S., Northcott, P.A., Grimmer, M.R., Lau, J., Chesler, L., Perry, A., et al. (2012). Distinct neural stem cell populations give rise to disparate brain tumors in response to N-MYC. *Cancer Cell* *21*, 601–613.
- Taylor, J., Kittappa, R., Leto, K., Gates, M., Borel, M., Paulsen, O., Spitzer, S., Karadottir, R.T., Rossi, F., Falk, A., and Smith, A. (2013). Stem cells expanded from the human embryonic hindbrain stably retain regional specification and high neurogenic potency. *J. Neurosci.* *33*, 12407–12422.
- Takashima, Y., Guo, G., Loos, R., Nichols, J., Ficiz, G., Krueger, F., Oxley, D., Santos, F., Clarke, J., Mansfield, W., et al. (2014). Resetting transcription factor control circuitry toward ground-state pluripotency in human. *Cell* *158*, 1254–1269.
- Taniguchi, H., He, M., Wu, P., Kim, S., Paik, R., Sugino, K., Kvitsiani, D., Fu, Y., Lu, J., Lin, Y., et al. (2011). A resource of Cre driver lines for genetic targeting of GABAergic neurons in cerebral cortex. *Neuron* *71*, 995–1013.
- Tiberi, L., Bonnefont, J., van den Ameel, J., Le Bon, S.D., Herpoel, A., Bilheu, A., Baron, B.W., and Vanderhaeghen, P. (2014). A BCL6/BCOR/SIRT1 complex triggers neurogenesis and suppresses medulloblastoma by repressing Sonic Hedgehog signaling. *Cancer Cell* *26*, 797–812.
- Vanner, R.J., Remke, M., Gallo, M., Selvadurai, H.J., Coutinho, F., Lee, L., Kushida, M., Head, R., Morrissy, S., Zhu, X., et al. (2014). Quiescent sox2(+) cells drive hierarchical growth and relapse in sonic hedgehog subgroup medulloblastoma. *Cancer Cell* *26*, 33–47.
- Visvader, J.E. (2011). Cells of origin in cancer. *Nature* *469*, 314–322.
- Vong, K.I., Leung, C.K.Y., Behringer, R.R., and Kwan, K.M. (2015). Sox9 is critical for suppression of neurogenesis but not initiation of gliogenesis in the cerebellum. *Mol. Brain* *8*, 25.
- Wassarman, K.M., Lewandoski, M., Campbell, K., Joyner, A.L., Rubenstein, J.L., Martinez, S., and Martin, G.R. (1997). Specification of the anterior hind-brain and establishment of a normal mid/hindbrain organizer is dependent on Gbx2 gene function. *Development* *124*, 2923–2934.
- Whyte, W.A., Orlando, D.A., Hnisz, D., Abraham, B.J., Lin, C.Y., Kagey, M.H., Rahl, P.B., Lee, T.I., and Young, R.A. (2013). Master transcription factors and mediator establish super-enhancers at key cell identity genes. *Cell* *153*, 307–319.

Wu, C.C., Hou, S., Orr, B.A., Kuo, B.R., Youn, Y.H., Ong, T., Roth, F., Eberhart, C.G., Robinson, G.W., Solecki, D.J., et al. (2017). mTORC1-Mediated Inhibition of 4EBP1 Is Essential for Hedgehog Signaling-Driven Translation and Medulloblastoma. *Dev. Cell* *43*, 673–688.e5.

Yan, K., Rousseau, J., Littlejohn, R.O., Kiss, C., Lehman, A., Rosenfeld, J.A., Stumpel, C.T.R., Stegmann, A.P.A., Robak, L., Scaglia, F., et al.; DDD Study; CAUSES Study (2017). Mutations in the Chromatin Regulator Gene BRPF1 Cause Syndromic Intellectual Disability and Deficient Histone Acetylation. *Am. J. Hum. Genet.* *100*, 91–104.

Yang, Z.J., Ellis, T., Markant, S.L., Read, T.A., Kessler, J.D., Bourbonlous, M., Schüller, U., Machold, R., Fishell, G., Rowitch, D.H., et al. (2008). Medulloblastoma can be initiated by deletion of Patched in lineage-restricted progenitors or stem cells. *Cancer Cell* *14*, 135–145.

You, L., Chen, L., Penney, J., Miao, D., and Yang, X.J. (2014). Expression atlas of the multivalent epigenetic regulator Brpf1 and its requirement for survival of mouse embryos. *Epigenetics* *9*, 860–872.

Yu, X., Ye, Z., Houston, C.M., Zecharia, A.Y., Ma, Y., Zhang, Z., Uygun, D.S., Parker, S., Vyssotski, A.L., Yustos, R., et al. (2015). Wakefulness Is Governed by GABA and Histamine Cotransmission. *Neuron* *87*, 164–178.

STAR★METHODS

KEY RESOURCES TABLE

REAGENT or RESOURCE	SOURCE	IDENTIFIER
Antibodies		
Anti-NeuN (1:2000)	Millipore	Cat# ABN78, RRID:AB_10807945
Anti-PCNA (1:2000)	Millipore	Cat# MAB424, RRID:AB_95106
Anti-Sox9 (1:2000)	Millipore	Cat# AB5535, RRID:AB_2239761
Anti-Sox2 (1:500)	Abcam	Cat# ab97959, RRID:AB_2341193
Anti-posphoH3 (1:500)	Abcam	Cat# ab97959, RRID:AB_2341193
Anti-Green Fluorescent Protein (1:200)	Thermo Fisher Scientific	Cat# A-11122, RRID:AB_221569
Anti-Doublecortin (1:500)	Millipore	Cat# AB2253, RRID:AB_1586992
Anti-Brpf1 (1:500)	Thermo Fisher Scientific	Cat# PA5-27783, RRID:AB_2545259
Anti-DYKDDDDK Tag (1:500)	Thermo Fisher Scientific	Cat# PA1-984B, RRID:AB_347227
Anti-Neuro D (A-10) (1:100)	Santa Cruz Biotechnology	Cat# sc-46684, RRID:AB_671759
Anti-Phospho-S6 Ribosomal Protein Ser235/236 (1:100)	Cell Signaling Technology	Cat# 2211, RRID:AB_331679
Anti-Phospho-Akt Ser473 (1:100).	Cell Signaling Technology	Cat# 4058, RRID:AB_331168
Alexa Fluor 488 goat anti-mouse (1:500)	Thermo Fisher Scientific	Cat# A28175, RRID:AB_2536161
Alexa Fluor 546 goat anti-rabbit (1:500)	Thermo Fisher Scientific	Cat# A-11010, RRID:AB_2534077
Alexa Fluor 647 goat anti-rabbit (1:500)	SouthernBiotech	Cat# 4030-31, RRID:AB_2795939
Alexa Fluor 488 goat anti-rabbit (1:500)	Thermo Fisher Scientific	Cat# A-11008, RRID:AB_143165
Alexa Fluor 488 goat anti-rat (1:500)	Thermo Fisher Scientific	Cat# A-11006, RRID:AB_2534074
Mouse IgG-heavy and light chain Biotinylated (1:250)	Bethyl	Cat# A90-116B, RRID:AB_309457
Anti-Synaptophysin - Clone 27G12	Leica Biosystems	Cat# NCL-L-SYNAP-299, RRID:AB_564017
Anti-Glial Fibrillary Acidic Protein (GFAP) - Clone GA5	Leica Biosystems	Cat# NCL-GFAP-GA5, RRID:AB_563739
Mouse Anti-Catenin, beta - Clone 14/Beta-Catenin	BD Transduction Laboratories	Cat# 610154, RRID:AB_397555
Anti-YAP1 (63.7)	Santa Cruz Biotechnology	Cat# sc-101199, RRID:AB_1131430
Anti-GAB1	Abcam	Cat# ab59362, RRID:AB_941700
Bacterial and Virus Strains		
10-beta Competent <i>E. coli</i> (High Efficiency)	NEB	Cat# C3019H
One Shot Stbl3 Chemically Competent <i>E. coli</i>	Invitrogen	Cat# C737303
Biological Samples		
Human adult SHH MB (nodular/desmoplastic) brain section from a 44-year-old female patient	Dr. Felice Giangaspero (University Sapienza of Rome)	N/A
Human adult SHH MB (nodular/desmoplastic) brain section from a 40-year-old male patient	Dr. Felice Giangaspero (University Sapienza of Rome)	N/A
Chemicals, Peptides, and Recombinant Proteins		
Poly-D-lysine	Sigma-Aldrich	Cat# P0899-50MG
Neurobasal medium	Thermo Fisher Scientific	Cat# 211103-049
Fetal Bovine Serum	Thermo Fisher Scientific	Cat# 10270106
D-(+)-Glucose	Sigma-Aldrich	Cat# G5767
Penicillin-Streptomycin (10,000 U/mL)	Thermo Fisher Scientific	Cat# 15140122
L-glutamine	GIBCO 100x	Cat# 25030081
Paraformaldehyde	Acros Organics	Cat#AC169650010
DMEM/F12	Thermo Fisher Scientific	Cat# 31330038
N-2 Supplement (100X)	Thermo Fisher Scientific	Cat# 17502048
B-27 Supplement (50X), serum free	Thermo Fisher Scientific	Cat# 17504044
EGF Recombinant Human Protein	Thermo Fisher Scientific	Cat# PHG0313

(Continued on next page)

Continued

REAGENT or RESOURCE	SOURCE	IDENTIFIER
FGF2-Basic Recombinant Human Protein	Thermo Fisher Scientific	Cat# PHG0264
8-Bromo-cAMP	Santa cruz	Cat# Sc-201564a
4-Hydroxytamoxifen	Sigma-Aldrich	Cat# H7904
Tamoxifen, 98% (50 mg/Kg)	Alfa Aesar	Cat# J63509
NucleoBond® Xtra Midi kits	Macherey-Nagel	Cat# 740410.50
NucleoSpin® Gel and PCR Clean-up	Macherey-Nagel	Cat# 740609.250
NucleoSpin® Plasmid (NoLid)	Macherey-Nagel	Cat# 740499.250
T4 DNA ligase (5 U/μL)	Thermo Fisher Scientific	Cat# EL0011
T4 DNA ligase Buffer (10X)	Thermo Fisher Scientific	Cat# B69
<i>in vivo</i> -jetPEI transfection reagent	Polyplus-transfection	Cat# 201-50G
Sucrose	Biosigma	Cat# S5016
bovine serum albumin (BSA)	SEQENS IVD / H2B	Cat# 1000-70
Triton X-100	Sigma-Aldrich	Cat# T8787
Normal Goat Serum	Sigma-Aldrich	Cat# S26
Hoechst	Abcam	Cat# 33258
Vectastain Elite ABC Kit Standard	Vector Labs	Cat# PK-6100
DAB Peroxidase Substrate Kit	Vector Labs	Cat# SK-4100
Hematoxylin	Abcam	Cat# ab220365
TRIZOL Reagent	Invitrogen	Cat# 15596018
iScript cDNA synthesis kit	Biorad	Cat# 1708891
Power SYBR Green PCR Master Mix	Thermo Fisher Scientific	Cat# 4367659
OptiPrep Density Gradient Medium (60% Iodixanol)	Sigma-Aldrich	Cat# D1556
Tween-20	Sigma-Aldrich	Cat# P9416
IGEPAL® CA-630	Sigma-Aldrich	Cat# I3021
Digitonin	Promega	Cat# G9441
2x TD reaction buffer from Nextera kit	Illumina	Cat# FC-121-1030
Nextera Tn5 Transposase	Illumina	Cat# FC-121-1030
MinElute PCR Purification Kit	QIAGEN	Cat# 28004
Next High-Fidelity 2 × PCR Master Mix	NEB	Cat# M0541L
Critical Commercial Assays		
Click-iT EdU imaging kit	Invitrogen	Cat# C10632
Deposited Data		
Raw and analyzed data (ATAC-seq)	This paper	GEO: GSE127733
Experimental Models: Cell Lines		
Primary <i>ex-vivo</i> cerebellar cell culture from P7 mice	This paper	N/A
Human AF22 neuroepithelial-like stem cells	Falk et al., 2012	N/A
Experimental Models: Organisms/Strains		
<i>M. musculus</i> : Rosa26-LSL-SmoM2-EYFP	The Jackson Laboratory	Cat# JAX:005130, RRID:IMSR_JAX:005130
<i>M. Musculus</i> : Rosa26-LSL-tdTomato	The Jackson Laboratory	Cat# JAX:007908, RRID:IMSR_JAX:007908
<i>M. musculus</i> : Ptch1 flox/flox	The Jackson Laboratory	Cat# JAX:012457, RRID:IMSR_JAX:012457
<i>M. musculus</i> : Math1-creER	The Jackson Laboratory	Cat# JAX:007684, RRID:IMSR_JAX:007684
<i>M. musculus</i> : Sox9 flox/flox	The Jackson Laboratory	Cat# JAX:013106, RRID:IMSR_JAX:013106
<i>M. musculus</i> : Math1-GFP	The Jackson Laboratory	Cat# JAX:013593, RRID:IMSR_JAX:013593
<i>M. musculus</i> : Etv1-creER	The Jackson Laboratory	Cat# JAX:013048, RRID:IMSR_JAX:013048
<i>M. musculus</i> : Foxn1 nude mice	The Jackson Laboratory	Cat# JAX:002019, RRID:IMSR_JAX:002019
<i>M. musculus</i> : Gabra6-cre	Dr. William Wisden (Imperial College London)	N/A

(Continued on next page)

Continued

REAGENT or RESOURCE	SOURCE	IDENTIFIER
Oligonucleotides		
PCR primers and shRNA target sequences are in Table S2	N/A	N/A
Recombinant DNA		
pNeuroD1-IRES-GFP	Guerrier et al., 2009	RRID:Addgene_61403
pNeuroD1-cre-IRES-GFP	This paper	N/A
pAAV-hsyn-flex-dsRed-shvgat	Yu et al., 2015	RRID:Addgene_67845
pAAV-hSyn1-cre	This paper	N/A
pPB CAG rtTA-IN	Takashima et al., 2014	RRID:Addgene_60612
pRCF-Brpf1	Dr. Jacques Côté (Laval University Cancer Research Center)	N/A
pPB-CAG-3xFlag-BRPF1-IRES-GFP	This paper	N/A
pPB-CAG-3xFlag-BRPF1-TR-IRES-GFP	This paper	N/A
pDZ264	Larson et al., 2011	RRID:Addgene_35193
pPB-CAG-LSL-MCS-IRES-GFP	This paper	N/A
pPB-CAG-LSL-tdTomato	This paper	N/A
pPB-CAG-LSL-BRPF1 TR-IRES-GFP	This paper	N/A
SmoM2 (W535L)-pcw107-V5	Martz et al., 2014	RRID:Addgene_64628
pPB-CAG-LSL-MCS-IRES-Venus	This paper	N/A
pPB-LSL-SmoM2-IRES-Venus	This paper	N/A
pR275 lenti-NeuroD1prom-CreERT2-WPRE	Dr. Franck Polleux (Columbia University)	N/A
pPB-hSyn1-MCS-IRES-Venus	This paper	N/A
pPB-hSyn1-creER-IRES-Venus	This paper	N/A
pCMVHahyPBase	Wellcome Sanger Institute, Cambridge UK	N/A
pCAG-GLI1	Tiberi et al., 2014	N/A
pSilencer2.1-CAG-Venus (pSCV2)	Dr. Franck Polleux (Columbia University)	N/A
pSCV2-sh1Gli1	This paper	N/A
pSCV2-sh1Gli2	This paper	N/A
pPB-CAG-Venus	This paper	N/A
pPB-CAG-MCS-IRES-GFP	This paper	N/A
Software and Algorithms		
ImageJ	NIH	https://imagej.nih.gov/ij/
Prism 6	GraphPad Software	https://www.graphpad.com/
Adobe Illustrator	Adobe	https://www.adobe.com/it/products/illustrator.html
Adobe Photoshop	Adobe	https://www.adobe.com/it/products/photoshop.html
FastQC	Brabham Bioinformatics	https://www.bioinformatics.babraham.ac.uk/projects/fastqc/
Trimmomatic	Bolger et al., 2014	N/A
Bowtie2	Langmead and Salzberg, 2012	N/A
SAMtools	Li et al., 2009	N/A
BEDtools version 2.24.0	Quinlan and Hall, 2010	https://bedtools.readthedocs.io/en/latest/
bedGraphToBigWig program	ENCODE	https://www.encodeproject.org/software/bedgraphtobigwig/
UCSC Genome Browser	N/A	http://genome.ucsc.edu/
HOMER software	Heinz et al., 2010	N/A

(Continued on next page)

Continued

REAGENT or RESOURCE	SOURCE	IDENTIFIER
TM4 MeV v4.9 software	MeV	http://mev.tm4.org/
BoxPlotR	N/A	http://shiny.chemgrid.org/boxplotr/
ngsplot 2.47	Shen et al., 2014	N/A
Enrichr	Chen et al., 2013; Kuleshov et al., 2016	N/A
GREAT	McLean et al., 2010	N/A
Gene set enrichment analysis (GSEA)	Subramanian et al., 2005	N/A
Rank Ordering Of Super-Enhancers (ROSE) tool	Whyte et al., 2013; Lovén et al., 2013	N/A
AffyQC module tool	Eijssen et al., 2013	N/A
affy package	Gautier et al., 2004	N/A
BrainArray custom CDF (mouse4302mmengcdf version 22)	Dai et al., 2005	N/A
rma normalization method	Irizarry et al., 2003	N/A
org.Mm.eg.db	Bioconductor	https://bioconductor.org/packages/release/data/annotation/html/org.Mm.eg.db.html
limma package	Ritchie et al., 2015	N/A
Database for Annotation, Visualization and Integrated Discovery (DAVID) Bioinformatics Resources v6.8	Huang et al., 2009	N/A
fgsea package (GSEA)	Subramanian et al., 2005; Sergushichev, 2016	N/A
KEGG Pathways dataset (mouse profile, accessed in January 2018)	N/A	https://www.genome.jp/kegg/
Gene Set Knowledgebase (GSKB)	Bioconductor	http://ge-lab.org/gskb
COMBAT normalization (inSilicoMerging package)	COMBAT	N/A
Gene Expression Omnibus (GEO)	NCBI	https://www.ncbi.nlm.nih.gov/geo/
Custom CDF (HuGene11stv1_Hs_ENTREZID, ver 22)	BrainArray	http://brainarray.mbni.med.umich.edu/Brainarray/Database/CustomCDF/CDF_download.asp
org.Hs.eg.db	Bioconductor	N/A
Ensembl database (accessed in January 2018)	N/A	http://www.ensembl.org/useast.ensembl.org/index.html?redirectsrc=/www.ensembl.org%2Findex.html
mouse4302.db	Bioconductor	N/A
hugene11sttranscriptcluster.db	Bioconductor	N/A
HOM_MouseHumanSequence.rpt	N/A	http://www.informatics.jax.org/
library(oligo)	Bioconductor	N/A
library(pd.mouse430.2)	Bioconductor	N/A
library(mouse4302.db)	Bioconductor	N/A
library(genefilter)	Bioconductor	N/A
library(pd.hugene.1.1.st.v1)	Bioconductor	N/A
library(hugene11sttranscriptcluster.db)	Bioconductor	N/A
library(sva)	Bioconductor	N/A
library(data.table)	CRAN	N/A
library(factoextra)	CRAN	N/A
library(pheatmap)	CRAN	N/A

LEAD CONTACT AND MATERIALS AVAILABILITY

Further information and requests for resources and reagents should be directed to and will be fulfilled by the Lead Contact, Luca Tiberi (luca.tiberi@unitn.it). Plasmids generated in this study are available upon request with Material Transfer Agreements

EXPERIMENTAL MODEL AND SUBJECT DETAILS

Mice

Rosa26-LSL-SmoM2 (#005130), *Rosa26-LSL-tdTomato* (#007908), *Ptch1^{fllox/fllox}* (#012457), *Math1-creER* (#007684), *Sox9^{fllox/fllox}* (#013106), *Math1-GFP* (#013593), *Etv1-creER* (#013048), nude mice (#002019) were purchased from The Jackson Laboratory. Males and females *Gabra6-cre;LSL-SmoM2* mice were analyzed at E16.5, P7, P14, P21, P28, 3 months, > 5 months. Males and females *Gabra6-cre;LSL-tdTomato* mice were analyzed at P0, P4, P7, P10, P14, P21. Males and females *Gabra6-cre;Ptch1^{fllox/+}* mice were analyzed at 3 months and > 5 months whereas males and females *Gabra6-cre;Ptch1^{fllox/fllox}* mice were analyzed at P14, 3 months and > 5 months. Males and females *Gabra6-cre;LSL-SmoM2;Sox9^{fllox/fllox}* mice were analyzed at 4 weeks and 3 months. Males and females *Gabra6-cre;LSL-tdTomato;Math1-GFP* mice were analyzed at P0 and P7. Males and females *Math1creER;LSL-SmoM2* mice were injected with tamoxifen at P5 or P21 and then analyzed at 1 months, 3 months and > 5 months. Males and females *Math1-creER;Ptch1^{fllox/+}* mice were injected with tamoxifen at P5 and analyzed at 4 months. Males and females *Etv1-creER;LSL-SmoM2* mice were transfected with pPB-BRPF1 TR at P90 and then injected with tamoxifen. Those mice were analyzed at 138 days post injection. Males and females *LSL-SmoM2* mice were analyzed at P14, P28, 3 months and > 5 months. Males and females *LSL-SmoM2* mice were transfected with pNeuroD1-cre, pNeuroD1-cre + BRPF1 TR or pNeuroD1-cre + BRPF1 WT, phSynI-cre or phSynI-cre + BRPF1 TR and analyzed at 40, 60 and 100 days post injection. We did not detect any sex dependent differences in all mice analyzed. We thank Prof. William Wisden for providing us with *Gabra6-cre* mice. Mice were housed in a certified Animal Facility in accordance with European Guidelines. Mice were monitored daily for neurological symptoms of brain tumors: weight loss, hydrocephalus, kyphosis, altered gait, lethargy; and euthanized immediately when recommended by veterinary and biological services staff members. The experiments were approved by the Italian Ministry of Health as conforming to the relevant regulatory standards.

Human Adult SHH Medulloblastoma Samples

Human adult medulloblastoma brain sections from a 44-year-old female patient and a 40-year-old male patient have been provided by prof. Giangaspero from Department of Radiologic, Oncologic and Anatomic Pathological Sciences, University Sapienza of Rome, Rome, Italy and IRCCS Neuromed, Pozzilli, Isernia, Italy.

Cell Lines and Primary Cell Cultures

Primary Ex Vivo Cerebellar Cell Cultures

Cerebella were dissected from P7 *LSL-SmoM2* mice (males and females) and cells were dissociated by pipetting in dissociation medium (81,8 mM Na₂SO₄, 30 mM K₂SO₄, 5,8 mM MgCl₂, 0,25 mM CaCl₂, 1 mM HEPES pH 7,4, 20 mM Glucose, 0,2 mM NaOH). Cells were nucleofected with 10 µg of total DNA in 100 µl of nucleofection buffer (5mM KCl, 15mM MgCl₂, 10 mM Glucose, 120 mM K₂HPO₄/KH₂PO₄, pH7.2), using the A-033 program and a Nucleofector 2b Device (Amaxa). For the nucleofection ten different combinations of plasmids were used.

- Combination 1: pPB CAG-IRES-GFP, pPB CAG-Venus, pPBBase;
- Combination 2: pPB CAG-BRPF1 WT-IRES-GFP, pPB CAG-Venus, pPBBase;
- Combination 3: pPB CAG-BRPF1 TR-IRES-GFP, pPB CAG-Venus, pPBBase;
- Combination 4: phSynI-cre, pPB CAG-IRES-GFP, pPB CAG-Venus, pPBBase;
- Combination 5: phSynI-cre, pPB CAG-BRPF1 WT-IRES-GFP, pPB CAG-Venus, pPBBase;
- Combination 6: phSynI-cre, pPB CAG-BRPF1 TR-IRES-GFP, pPB CAG-Venus, pPBBase;
- Combination 7: phSynI-cre, pCAG-GLI1, pPB CAG-IRES-GFP, pPB CAG-Venus, pPBBase;
- Combination 8: phSynI-cre, pPB CAG-BRPF1 WT-IRES-GFP, pPB CAG-Venus, pCAG-GLI1, pPBBase;
- Combination 9: phSynI-cre, pPB CAG-IRES-GFP, pPB CAG-Venus, psh1-Gli1, psh1-Gli2, pPBBase;
- Combination 10: phSynI-cre, pPB CAG-BRPF1 TR-IRES-GFP, pPB CAG-Venus, psh1-Gli1, psh1-Gli2, pPBBase.

Nucleofected cells were plated in poly-D-lysine coated 24-well plates (each cerebellum was used to fill 4 wells) and grown in Neurobasal medium supplemented with: 20% FBS, 3 mM KCl, 2,1 mg/ml glucose, penicillin/streptomycin and 2mM L-glutamine. Medium was partially changed every 3 days. Cells were fixed after 7 days of growth using PFA 4%.

AF22 Cell Cultures

Human iPSC-derived neuroepithelial-like stem cells AF22 at passage 30, were cultured in a 1:1 ratio mixture of Neurobasal and DMEM/F12 media supplemented with N2 (1:100), B27 (1 µl/ml), 10 ng/ml EGF and 10 ng/ml FGF2. 2x10⁶ AF22 cells were nucleofected with 20 µg plasmid DNA in 200 µl nucleofection buffer using the T-020 program and a Nucleofector 2b device (Amaxa). AF22 cells were differentiated into neurons as previously described (Falk et al., 2012). Briefly, neurons were induced culturing the cells for three weeks in a 1:1 ratio mixture of Neurobasal and DMEM/F12 media supplemented with N2 (1:100), B27 (1:50) and 300 ng/ml cAMP. After 19 days of differentiation, 500 ng/ml 4-Hydroxytamoxifen was added to the differentiation media. Two days later neurons were collected for downstream analyses. Four nucleofection plasmid combination were tested.

- Combination 1: pPB-hSynl-creER, pPB-CAG-LSL-tdTomato, pPBBase;
Combination 2: pPB-hSynl-creER, pPB-CAG-LSL-tdTomato, pPB-LSL-SmoM2, pPBBase;
Combination 3: pPB-hSynl-creER, pPB-CAG-LSL-tdTomato, pPB-LSL-BRPF1 TR, pPBBase;
Combination 4: pPB-hSynl-creER, pPB-CAG-LSL-tdTomato, pPB-LSL-SmoM2, pPB-LSL-BRPF1 TR, pPBBase.

METHOD DETAILS

Plasmids

The coding sequence of Cre recombinase was cloned into pNeuroD1-IRES-GFP creating pNeuroD1-cre-IRES-GFP. pNeuroD1-IRES-GFP is a gift from Franck Polleux (Guerrier et al., 2009) (Addgene plasmid # 61403). The coding sequence of cre recombinase was cloned into pAAV-hsyn-flex-dsRed-shvgtat (Yu et al., 2015) (Addgene#67845), forming pAAV-hSynl-cre (phSynl-cre). The coding sequence of human BRPF1 was amplified by PCR from a plasmid of Dr. Jacques Côté (Laval University Cancer Research Center, Canada) and cloned into pPB CAG rtTA-IN (Takashima et al., 2014) (Addgene #60612), forming pPB-CAG-3xFlag-BRPF1-IRES-GFP (pPB-BRPF1 WT). Truncated human BRPF1 was amplified by PCR from WT 3xFlag-BRPF1 (1-574aa) and cloned into pPB-CAG rtTA-IN (Takashima et al., 2014) (Addgene #60612) forming pPB-CAG-3xFlag-BRPF1-TR-IRES-GFP (pPB-BRPF1 TR). The coding sequence of tdTomato was amplified by PCR from pDZ264 (Larson et al., 2011) (Addgene#35193) and cloned into pPB-CAG-LSL-MCS-IRES-GFP, forming pPB-CAG-LSL-tdTomato. Truncated human BRPF1 was amplified by PCR from pPB-CAG-3xFlag-Brpf1-TR-IRES-GFP and cloned into pPB-CAG-LSL-MCS-IRES-GFP, forming pPB-CAG-LSL-BRPF1 TR-IRES-GFP (pPB-LSL-BRPF1 TR). The coding sequence of human SmoM2 was amplified by PCR from SmoM2 (W535L)-pcw107-V5 (Martz et al., 2014) (Addgene#64628) and cloned into pPB-CAG-LSL-MCS-IRES-Venus, forming pPB-LSL-SmoM2-IRES-Venus (pPB-LSL-SmoM2). The coding sequence of creER^{T2} was cloned from pR275 lenti-NeuroD1prom-CreERT²-WPRE (gift from Franck Polleux) and cloned into pPB-hSynl-MCS-IRES-Venus, forming pPB-hSynl-creER-IRES-Venus (pPB-hSynl-creER). The plasmid encoding a hyperactive form of the piggyBac transposase, pCMVHahyPBase (PBase) was provided from the Wellcome Sanger Institute, Cambridge UK. The plasmid encoding the overexpression of GLI1 transcription factor (pCAG-GLI1) was provided by Tiberi et al. (2014). Double-stranded oligonucleotides coding for mouse Gli1 shRNA (target sequence, 5'- TCGGAGTTCAGTCAAATTA -3') (Tiberi et al., 2014), mouse Gli2 shRNA (target sequence, 5'- AATGATGCCAACCAGAACAAG -3') (Tiberi et al., 2014) were cloned downstream of the U6 promoter into the pSilencer2.1-CAG-Venus (pSCV2) (gift from Franck Polleux) according to the pSilencer instructions from Ambion, forming pSCV2-sh1Gli1 and pSCV2-sh1Gli2. Venus was amplified from pSCV2, to generate pPB-CAG-Venus plasmid (pPB-Venus). The backbone pPB-CAG-MCS-IRES-GFP (pPB-GFP) was used as readout of nucleofection efficiency in *ex vivo* cerebellar assay. All plasmid used for *in vivo* transfection, *ex vivo* nucleofection and AF22 cell culture; pNeuroD1-cre-IRES-GFP (pNeuroD1-cre), pAAV-hSynl-cre (phSynl-cre), pPB-CAG-3xFlag-Brpf1-IRES-GFP (pPB-BRPF1 WT), pPB-CAG-3xFlag-Brpf1-TR-IRES-GFP (pPB-BRPF1 TR), pPB-CAG-LSL-BRPF1-TR-IRES-GFP (pPB-LSL-BRPF1 TR), pPB-LSL-SmoM2-IRES-Venus (pPB-LSL-SmoM2), pPB-hSynl-creER-IRES-Venus (pPB-hSynl-creER), pPB-CAG-LSL-tdTomato, pPB-CAG-IRES-GFP (pPB-GFP), pPB-CAG-Venus (pPB-Venus), pCAG-GLI1, pSCV2-sh1Gli1 (psh1-Gli1), pSCV2-sh1GLI2 (psh2-Gli2), pCMV-HahyPBase (PBase) are purified using the NucleoBond® Xtra Midi kits (Macherey-Nagel).

In Vivo Transfection of Granule Neurons

A mix of plasmid DNA (0.5 µg/µl) and *in vivo*-jetPEI transfection reagent (Polyplus-transfection) was prepared according to the manufacturer's instructions. pPBBase and piggyBac donor plasmids were mixed at a 1:4 ratio. P21-24 and 2, 3-month-old *LSL-SmoM2* mice (males and females) were anaesthetised with 2% isoflurane and medially injected at -1.6 mm rostral to lambda, 0 mm midline, and 1 mm ventral to the skull surface, with 10 µL of DNA transfection reagent mix using a Syringe with a 30-gauge needle.

Transplantation of Tumor Cells in Nude Mice

Tumor of 4-month-old *Gabra6-cre;LSL-SmoM2* mouse was single cell dissociated in trypsin and resuspended in Neurobasal medium at a concentration of 3.2×10^{-4} cells/µl. For transplantation, 4-month-old nude mice (males and females) were anaesthetised with 2% isoflurane and medially injected at -1.6 mm rostral to lambda, 0 mm midline, and 1 mm ventral to the skull surface, with 10 µL of freshly isolated tumor cells using a 26 s-gauge Hamilton syringe. The cells were injected slowly, and the incision was sutured with one or two drops of medical glue. Animals were monitored for 50 days post-transplantation; brains were fixed by perfusion with 4% paraformaldehyde and then appropriately cryoprotected in 30% sucrose (wt/vol, Merck).

Histopathological Evaluation

Three *Gabra6-cre;LSL-SmoM2* tumors were diagnosed by neuropathologists Francesca Gianno and Felice Giangaspero. In addition to standard hematoxylin and eosin staining, immunostaining was done on formalin-fixed paraffin-embedded tumors after dewaxing and rehydrating slides. Antigen retrieval was performed by incubating slices in citrate based pH 6.0 epitope retrieval solution. Primary antibodies were incubated overnight at 4°C and secondary antibodies for 1 hour at room temperature in Antibody solution. ABC solution was used 2 hours at room temperature (Vectastain Elite ABC Kit Standard PK-6100). The sections were incubated with the

substrate at room temperature until suitable staining was observed (DAB Peroxidase Substrate Kit, SK-4100). Nuclei were counterstained with Hematoxylin (Abcam, ab220365).

Immunofluorescence

E16.5, P0, P4, P7, P10, P14, P21, P28, 3, 4, 7-month-old mice (males and females) were perfused with 4% paraformaldehyde and then brains were cryoprotected in 30% sucrose (wt/vol, Merck). Immunofluorescence stainings were performed on slides, 20/30- μ m-thick cryosections. Blocking and Antibody solutions consisted of PBS supplemented with 3% goat serum, 0.3% Triton X-100 (Sigma). Primary antibodies were incubated overnight at 4°C and secondary for 1 h at 15–25°C. Nuclei were stained with bisbenzamide (Hoechst#33258, Sigma). Sections and coverslips were mounted with Permanent Mounting Medium (PMT030).

EdU Staining

P19 *Gabra6-cre;LSL-SmoM2* and *Gabra6-cre;LSL-tdTomato* mice (males and females) were i.p. injected with 50 mg/kg EdU and sacrificed at P21. EdU staining was conducted on brain slices, using Click-iT EdU imaging kit (Invitrogen, Carlsbad, CA), according to the manufacturer's protocol. This protocol was adapted for histological staining of brain tissue as follows. Slides containing mounted frozen brain sections were fixed with 4% paraformaldehyde in phosphate buffer saline (PBS) for 15 min. Fixation step is required to maintain previous staining since EdU labeling has to be performed later. Slides were washed with 3% bovine serum albumin (BSA) in PBS and then permeabilized with 0.5% Triton X-100 in PBS for 20 min. The sections were again washed with 3% BSA in PBS and then incubated with a Click-iT reaction cocktail containing PBS 1X, 4 mM CuSO₄, Alexa Fluor® 488 Azide, and reaction buffer additive for 30 min, while protected from light. The sections were washed once more with 3% BSA in PBS and the incubated with Hoechst (#33258) for DNA staining.

Imaging

Images were acquired with a Zeiss Axio Imager M2 (AxioCam MRc, AxioCam MRm), and Zeiss Axio Observer Z1 equipped with Colibri 1, ApoTome 1 and Cell Observer modules. Confocal imaging was performed with either Leica TCS Sp5 or NIKON Eclipse Ti2 Spinning Disk confocal Imager optical. Images were processed using ImageJ software. Figures were prepared using Adobe Photoshop (Adobe).

Cell Quantification

For quantification of Sox9/Sox2/PCNA positive cells in 4-week-old *Gabra6-cre;LSL-SmoM2* mice, we used at least three sections of each brain (three brains for each marker), quantified cells: 101 Sox9⁺/Hoechst⁺ cells within 2700 Hoechst positive cells, 119 Sox2⁺/Hoechst⁺ cells within 2700 Hoechst positive cells, 2672 PCNA⁺/Hoechst⁺ cells within 2700 Hoechst positive cells. For quantification of Edu and NeuN double positive cells, we used at least three sections in three different brains, quantified cells: 79 Edu⁺/NeuN⁺ cells within 900 Edu positive cells in *Gabra6-cre;LSL-SmoM2* mice, 0 Edu⁺/NeuN⁺ cells within 477 Edu positive cells in *Gabra6-cre;LSL-tdTomato* mice. For quantification of Edu and tdTomato double positive cells, we used at least three sections in three different brains of *Gabra6-cre;LSL-tdTomato*, quantified cells: 0 Edu⁺/tdTomato⁺ cells within 368 Edu positive cells. For quantification of tdTomato and PCNA double positive cells we have used at least six sections of each brain (three brains for each time point), we quantified: P4 = 927 tomato positive cells, P7 = 9145 tomato positive cells, P10 = 42940 tomato positive cells, P14 = 106090 tomato positive cells. For quantification of tdTomato and pH3 double positive cells we have used at least six sections of each brain (three brains for each time point), we quantified: P4 = 4786 ph3 positive cells, P7 = 842 ph3 positive cells, P10 = 1676 ph3 positive cells, P14 = 350 ph3 positive cells. For quantification of tdTomato and Sox2 double positive cells we have used at least six sections of each brain (three brains for each time point), we quantified: P10 = 8905 sox2 positive cells, P14 = 8422 sox2 positive cells. For quantification of tdTomato and Sox9 double positive cells we have used at least six sections of each brain (three brains for each time point), we quantified: P10 = 7953 sox9 positive cells, P14 = 8061 sox9 positive cells. To identify the tomato positive cells *Rosa26-CAG-LSL-tdTomato* mice without cre have been used to detect background levels. For quantification of tdTomato and GFP double positive cells in *Gabra6-cre;Math1-GFP;LSL-tdTomato* mice, we used at least three sections of each brain (three brains for each time point), quantified cells: P0 = 0 GFP⁺/tdTomato⁺ cells within 41 tdTomato positive cells, P7 = 0 GFP⁺/tdTomato⁺ cells within 1805 tdTomato positive cells. For quantification of Sox9/Sox2/PCNA and GFP double positive cells in P21 *Rosa26-CAG-LSL-SmoM2* mice transfected with pNeuroD1-cre-IRES-GFP at least three sections of each brain have been used (three brains for each marker), quantified cells: GFP⁺/Sox9⁺ = 0 cells, GFP⁺/Sox9⁻ = 1105 cells, GFP⁺/Sox2⁺ = 0 cells, GFP⁺/Sox2⁻ = 978 cells, GFP⁺/PCNA⁺ = 0 cells, GFP⁺/PCNA⁻ = 1182 cells. For quantification of Sox9/Sox2/PCNA/pH3 and tdTomato double positive cells in 2-month-old *Rosa26-CAG-LSL-SmoM2* mice transfected with phSyn1-cre and pPB-CAG-LSL-tdTomato at least three sections of each brain have been used (three brains for each marker), quantified cells: tdTomato⁺/Sox9⁺ = 0 cells, tdTomato⁺/Sox9⁻ = 2361 cells, tdTomato⁺/Sox2⁺ = 0 cells, tdTomato⁺/Sox2⁻ = 819 cells, tdTomato⁺/PCNA⁺ = 0 cells, tdTomato⁺/PCNA⁻ = 1139 cells, tdTomato⁺/pH3⁺ = 0 cells, tdTomato⁺/pH3⁻ = 2005 cells. For quantification of Sox9/Sox2/PCNA/pH3 and tdTomato double positive cells in 3-month-old *Etv1cre-ER;LSL-SmoM2* mice transfected with pPB-CAG-LSL-tdTomato at least three sections of each brain have been used (three brains for each marker), quantified cells: tdTomato⁺/Sox9⁺ = 0 cells, tdTomato⁺/Sox9⁻ = 390 cells, tdTomato⁺/Sox2⁺ = 0 cells,

tdTomato⁺/Sox2⁻ = 532 cells, tdTomato⁺/PCNA⁺ = 0 cells, tdTomato⁺/PCNA⁻ = 410 cells, tdTomato⁺/pH3⁺ = 0 cells, tdTomato⁺/pH3⁻ = 570 cells. For the quantification of the nucleofected *ex vivo* cerebellar cells, we quantified at least 300 cells GFP+NeuN+ cells for each condition from three biological repeats. The background levels of GFP/YFP have been detected in cerebellar cells nucleofected without plasmids.

RNA Isolation and Real-Time PCR Analysis

Total RNA from samples were isolated with TRIzol Reagent (Invitrogen) and reverse transcribed using iScript cDNA synthesis kit (Bio-rad) according to the manufacturer's instructions. Quantitative PCR was performed using Power SYBR Green PCR Master Mix (Applied Biosystems).

Survival Analysis

Survival analysis was performed calculating the lifespan in days of every *Rosa26-LSL-SmoM2*, *Gabra6-cre*; *Rosa26-LSL-SmoM2* and *Rosa26-LSL-SmoM2* mouse transfected with each specific combination of plasmids. Kaplan-Meier survival curves (Figures 4D and 5F) do not take in consideration *LSL-SmoM2* mice transfected with pNeuroD1-cre+BRPF1-TR (Figure 4C) and phSynl-cre+BRPF1-TR which were sacrificed at a fixed experimental endpoint. Mice died due to undetermined causes during the study were censored in the analysis.

ATAC-Seq

ATAC-Seq Samples Preparation

We performed ATAC-seq on frozen cerebella from P14 *Gabra6-cre*;*LSL-SmoM2* and control *Gabra6-cre* mice and on hSynl-creER+LSL-tdTomato, hSynl-creER+LSL-BRPF1 TR, hSynl-creER+LSL-SmoM2 and hSynl-creER+LSL-SmoM2+LSL-BRPF1 TR nucleofected AF22 neuroepithelial-like stem cells, as previously described (Corces et al., 2017). Briefly, we first dounced frozen cerebella in 2 mL cold homogenization buffer (0.017 mM PMSF, 0.17 mM β-mercaptoethanol, 320 mM sucrose, 0.1 mM EDTA, 0.1% NP40, 5 mM CaCl₂, 3 mM Mg(Ac)₂, 10 mM Tris pH 7.8) and pelleted at 100 RCF for 1 min. We next isolated nuclei by transferring 400 ul of supernatant in a plastic tube and sequentially added 400 ul of 50% Iodixanol solution (homogenization buffer and 50% Iodixanol solution), 600 ul of 29% Iodixanol (homogenization buffer, 160 mM and 29% Iodixanol solution) and 600 ul of 35% Iodixanol solution (homogenization buffer, 160 mM and 35% Iodixanol solution) to the bottom of the tube, avoiding mixture of layers. At this point cell lines were also processed in order to isolate their nuclei. We centrifuged for 20 min at 3,000 RCF and we discarded upper layers of the gradient in order to collect 200 ul from the nuclei band. We counted nuclei and transferred 50.000 into a tube with 1 mL of ATAC-Resuspension Buffer (RSB) + 0.1% Tween-20 (10 mM Tris-HCl pH 7.4, 10 mM NaCl, 3 mM MgCl₂, 0.1% Tween-20). We pelleted nuclei by centrifuging for 10 minutes at 500 RCF and resuspended in 50 ul cold ATAC-RSB containing 0.1% NP40, 0.1% Tween-20, and 0.01% Digitonin,. We lysed for 3 minutes on ice and washed with 1 mL of cold ATAC-RSB + 0.1% Tween-20. We then transposed the samples by resuspending in 50 ul of transposition mix (25 ul 2x TD buffer, 100nM transposase, 16.5 ul PBS, 0.5 ul 1% digitonin, 0.5 ul 10% Tween-20, 5 ul H₂O) and incubated at 37°C for 30 minutes. We purified the transposed DNA using the QIAGEN MinElute PCR Purification Kit (cat. # 28004) and eluted in 10 μL elution buffer. Next we amplified the transposed DNA fragments in the PCR mix (10 μL transposed DNA, 10 μL nuclease-free H₂O, 2.5 μL 25 μM PCR Primer 1, 2.5 μL 25 μM Barcoded PCR Primer 2 and 25 μL NEB Next High-Fidelity 2 × PCR Master Mix cat. # M0541L). The final ATAC-seq libraries were purified using the QIAGEN MinElute PCR Purification Kit, quantified at the Qubit Fluorometer (Invitrogen, cat. #Q33226) and quality controlled with the High Sensitivity DNA Assay at the 2100 Bioanalyzer (Agilent, cat. # G2939BA). Four and three independent biological replicates, sequenced as independent libraries, were performed for *Gabra6-cre*;*LSL-SmoM2* and control *Gabra6-cre*, respectively. Two independent biological replicates, sequenced as independent libraries, were performed for hSynl-creER+LSL-tdTomato, hSynl-creER+LSL-BRPF1 TR, hSynl-creER+LSL-SmoM2 and hSynl-creER+LSL-SmoM2+LSL-BRPF1 TR cell lines. All libraries were sequenced as single reads of 50 bp with the Illumina HiSeq2500.

ATAC-Seq Data Processing

Sequenced reads from all independent sequenced libraries were quality assessed by using fastQC (<https://www.bioinformatics.babraham.ac.uk/projects/fastqc/>) and trimmed with Trimmomatic (Bolger et al., 2014). Reads from biological replicates were merged for all analysis, unless differentially stated in figure legends. Total reads were aligned to either the mouse genome NCBI37/mm9 or the human genome GRCh37/hg19 using Bowtie2 (Langmead and Salzberg, 2012), using the parameters '-very-sensitive -k 1', thus discarding ambiguous reads mapping at multiple sites. Duplicated reads and reads mapping on mitochondrial DNA were discarded for further analysis with SAMtools (Li et al., 2009). Normalized BigWig tracks of ATAC-seq signals were generated with BEDtools 2.24.0 (<https://bedtools.readthedocs.io/en/latest/>) (Quinlan and Hall, 2010) and the bedGraphToBigWig program (<https://www.encodeproject.org/software/bedgraphtobigwig/>) and visualized on the UCSC Genome Browser (<http://genome.ucsc.edu/>). The HOMER software (Heinz et al., 2010) was further used to analyze ATAC-seq data. The command 'findPeaks' was used for peak calling with these parameters '-size 150 -minDist 1000'; the command 'get-DifferentialPeaks' was used to find peaks with differential ATAC-seq signals between two conditions ('-F 2 -P 0.001'); the command 'findMotifsGenome.pl' was used for motifs enrichment analysis; the command 'annotatePeaks.pl' was used to annotate peaks to related genes and genomic regions and to count the

number of normalized reads on specific regions. Tag counts were then used to produce heatmaps with TM4 MeV v4.9 software (<http://mev.tm4.org/>) and boxplots with BoxPlotR (<http://shiny.chemgrid.org/boxplotr/>). Average tag density plot of the normalized (RPM) ATAC-seq signals were generated with the ngsplot 2.47 (Shen et al., 2014) command ngs.plot.r and plotted with GraphPad Prism (GraphPad Software, San Diego, California, USA, <https://www.graphpad.com>). Annotated genes were checked for biological processes and pathways enrichment using both Enrichr (Chen et al., 2013; Kuleshov et al., 2016) and GREAT (McLean et al., 2010). Gene set enrichment analysis was performed with GSEA (Subramanian et al., 2005) on publicly available gene sets. Super-enhancers were called with the Rank Ordering Of Super-Enhancers (ROSE) tool (Lovén et al., 2013; Whyte et al., 2013), using the ATAC-seq signal and with default parameters.

Microarray Analysis

Differential Gene Expression Analysis

As a first step, we checked the quality of the raw data file (CEL file) using the AffyQC module tool (Eijssen et al., 2013) observing that the quality indicator values were within the recommended thresholds. Then we follow the quantification procedures using a standard workflow: raw data files were processed with affy package (Gautier et al., 2004) using BrainArray custom CDF (Dai et al., 2005) (mouse4302mmengcdf version 22) and normalized/summarized using rma method (Irizarry et al., 2003). The additional gene annotation was retrieved using org.Mm.eg.db package (<https://bioconductor.org/packages/release/data/annotation/html/org.Mm.eg.db.html>). To obtain the differential gene list, we used the principles of linear models and empirical bayes methods as implemented in the limma package (Ritchie et al., 2015). In this way we obtained a list of 1183 differential expressed genes (absolute log fold change greater than 1.5 and multiple-testing adjusted p values < 0.05 (Benjamini and Hochberg, 1995). The functional annotation was performed using two approaches: a) the upregulated genes or downregulated genes (Huang et al., 2009) were analyzed separately through the Database for Annotation, Visualization and Integrated Discovery (DAVID) Bioinformatics Resources v6.8 using the stringent parameter set equal to “high” and the background parameter set to match the actual microarray platform. b) Gene set enrichment analysis was performed using the version implemented in fgsea package (Sergushichev, 2016; Subramanian et al., 2005) performing 10000 permutations and using as database the combination of the KEGG Pathways dataset (mouse profile, accessed in January 2018) and the Gene Set Knowledgebase (GSKB), a comprehensive knowledgebase for pathway analysis in mouse (for detail see <http://ge-lab.org/gskb>).

Gene Expression Comparison

Mouse comparison. We download from Gene Expression Omnibus the raw data from different datasets (GEO: GSE11859, GSE24628, GSE33199) comprehending several types of Medulloblastoma mouse models as well normal cerebellum tissues. The low level analysis was performed as described above. To remove the possible batch bias and compare these samples to our data, we performed COMBAT normalization as implemented in inSilicoMerging package (Johnson et al., 2007). Then we performed Classical Multidimensional Scaling of all merged datasets, plotting the results of the two principal coordinates.

Human comparison. We download from Gene Expression Omnibus the raw data of the GEO: GSE85217 dataset. The low level analysis was performed as described above with the differences of the used custom CDF (HuGene11stv1_Hs_ENTREZID, ver 22) and the annotation package (org.Hs.eg.db). Then we used the human-mouse orthologs mapping information from the Ensembl database (accessed in January 2018) to re-annotate the mouse dataset into human identifiers. Also in this case, we used the COMBAT normalization method to reduce the differences between platforms and organisms. Then we calculated the median values of the Sonic Hedgehog Pathway genes using the human gene list from KEGG database.

Similarity of Mouse and Human Adult SHH MB

Our pNeuroD1-cre+BRPF1 TR, phSyn1-cre+BRPF1 TR and *Gabra6-cre;LSL-SmoM2* mice data and *Math1-cre;LSL-SmoM2* mice data (GEO: GSE11859) were combined with human adult and infant SHH MB data (GEO: GSE85217). As previously described, data was normalized using rma method and COMBAT was used to remove potential batch bias. Annotation for mouse data was obtained using mouse4302.db package while annotation for human data was obtained using hugene11sttranscriptcluster.db package. Human-mouse orthologs mapping was performed using HOM_MouseHumanSequence.rpt table available from www.informatics.jax.org. Hierarchical clustering using differential expressed genes from Al-Halabi et al. (2011), with observed absolute log₂ fold change greater than 2 was performed using Pearson's correlation coefficient as distance measure. Clustering analysis was performed on samples.

QUANTIFICATION AND STATISTICAL ANALYSIS

Statistical Analysis

Quantitative Real-Time-PCR Analysis

Data are presented as mean + s.e.m. of three biologically independent P14 cerebella (Figure S3A) or differentiated AF22 cells (Figure S6H). Two-tailed Student's t test was used for calculating significance values.

Ex Vivo Cerebellar Cell Cultures

Data are presented as mean + s.e.m. of three biologically independent ex vivo experiments. Two-tailed Student's t test was used for calculating significance values. PiggyBac n = 1733 cells, BRPF1 WT n = 1841 cells, BRPF1 TR n = 1637 cells, hSyn1-cre n = 1185

cells, hSyn1-cre+BRPF1 WT = 1321 cells, hSyn1-cre+BRPF1 TR = 837 cells, hSyn1-cre+BRPF1 WT+GLI1 n = 4238 cells, hSyn1-cre+GLI1 n = 2156 cells, hSyn1-cre+shGli1+shGli2 n = 3796, hSyn1-cre+BRPF1 TR+shGli1+shGli2 n = 3505 (Figure S5J).

Survival Statistical Analysis

Data were displayed using the Kaplan-Meier format and statistical significance of the results was tested using the Log-rank (Mantel-Cox) test. *Gabra6-cre;LSL-SmoM2* n = 23 mice, *LSL-SmoM2* n = 11 mice (Figure 1C); pNeuroD1-cre + BRPF1 TR n = 17 mice, pNeuroD1-cre + BRPF1 WT n = 19 mice (Figure 4D); phSyn1-cre + BRPF1 TR n = 12 mice, phSyn1-cre n = 22 mice (Figure 5F).

DATA AND CODE AVAILABILITY

The data discussed in this publication have been deposited in NCBI's Gene Expression Omnibus (GEO). The accession number for the ATAC-seq data reported in this paper is GEO: GSE127733.